# Caveolae govern plasma membrane mechanics to protect cells against EDIN B-induced transcellular tunnel formation and lethality from S. aureus septicaemia

Camille Morel, Eline Lemerle, Feng-Ching Tsai, Thomas Obadia, Nishit Srivastava, Maud Marechal, Audrey Salles, Marvin Albert, Caroline Stefani, Christophe Lamaze, et al.

# Caveolae govern plasma membrane mechanics to protect cells against EDIN B-induced transcellular tunnel formation and lethality from *S. aureus* septicaemia

**Authors**

Camille Morel[1], Eline Lemerle[2], Feng-Ching Tsai[3], Thomas Obadia[4,5], Nishit Srivastava[6], Maud Marechal[1], Audrey Salles[7], Marvin Albert[8], Caroline Stefani[9], Christophe Lamaze[10], Stéphane Vassilopoulos[2], Matthieu Piel[6], Patricia Bassereau[3], David Gonzalez-Rodriguez[11], Cécile Leduc[12*], Emmanuel Lemichez[1*]

**Affiliations**

[1] Institut Pasteur, Université Paris Cité, CNRS UMR6047, INSERM U1306, Bacterial Toxins Unit, Department of Microbiology, F-75015 Paris, France.
[2] Sorbonne Université, INSERM UMR U974, Institut de Myologie, Centre de Recherche en Myologie, F-75013 Paris, France.
[3] Institut Curie, PSL Research University, CNRS UMR168, Laboratoire Physico-Chimie Curie, F-75005 Paris, France.
[4] Institut Pasteur, Université Paris Cité, Bioinformatics and Biostatistics Hub, F-75015 Paris, France.
[5] Institut Pasteur, Université Paris Cité, G5 Infectious Diseases Epidemiology and Analytics, F-75015, Paris, France.
[6] Institut Curie and Institut Pierre Gilles de Gennes, PSL Research University, Sorbonne University, CNRS UMR144, F-75005 Paris, France.
[7] Institut Pasteur, Université de Paris Cité, Unit of Technology and Service Photonic BioImaging (UTechS PBI), C2RT, F-75015 Paris, France.
[8] Institut Pasteur, Université Paris Cité, Image Analysis Hub, F-75015 Paris, France.
[9] Benaroya Research Institute at Virginia Mason, Department of Immunology, Seattle, USA.
[10] Institut Curie, PSL Research University, INSERM U1143, CNRS UMR3666, Membrane Mechanics and Dynamics of Intracellular Signaling Laboratory, F-75005 Paris, France.
[11] Université de Lorraine, LCP-A2MC, F-57000 Metz, France.
[12] Institut Jacques Monod, Université Paris Cité, CNRS UMR7592, F-75013 Paris, France.

*: corresponding authors: emmanuel.lemichez@pasteur.fr and cecile.leduc@ijm.fr

## Abstract

The spontaneous opening of large transendothelial cell macroaperture (TEM) tunnels can accompany leukocyte diapedesis and is triggered by bacterial exoenzymes that inhibit RhoA-driven cytoskeleton contractility. Modelling the dynamics of TEM via a theoretical framework used for soft matter physics allowed us to depict the essential driving forces at play on the membrane to enlarge TEMs. In this study, we conducted multidisciplinary experiments to characterize the role respectively played by cavin-1-structured caveolae and non-caveolar caveolin-1 in plasma membrane mechanics and identify their functional effects on TEM size. The results pointed towards

a contributing role for non-caveolar caveolin-1 in the membrane bending rigidity, a mechanical parameter we quantified in a model system of tubes pulled from plasma membrane spheres. Depletion of cavin-1-structured caveolae showed no effect on membrane rigidity, whereas caveolae controlled cell height favouring TEM nucleation. Hence, caveolae confer protection against exoenzyme EDIN-B in mice with staphylococcal septicaemia.

# MAIN TEXT

## Introduction

The endothelium lining the inner surface of the vasculature is an active monolayer that senses haemodynamic forces, enabling proper control of plasma membrane mechanical properties and barrier function (*1, 2*). Regulation of the endothelial barrier involves paracellular exchanges at both cell–cell junctions (*3*) and less-characterized transcellular exchanges realized via membrane pores that are 60-80 nm in diameter and large gaps between transendothelial cells that are several micrometres wide (*4*). Transcellular pores, which contribute to aqueous humour outflow and the diapedesis of leukocytes, show homology with transendothelial cell macroaperture (TEM) tunnels, the formation of which is triggered by several bacterial exoenzymes and toxins that breach the endothelial barrier, inducing oedema and haemorrhage, as well as promoting systemic dissemination of *Staphylococcus aureus* (*5–7*).

Large-scale membrane deformation induced by pathogenic bacteria and their toxins is key to the aetiology of infections. A group of exotoxins from pathogenic bacteria can trigger TEM tunnels with typical diameters ranging from 10 to 20 µm (*8–10*). This group of TEM tunnel-forming toxins includes *Clostridium botulinum* exoenzyme C3 (ExoC3), which is representative of bacterial ADP ribosyltransferases that inhibit the small GTPase RhoA. ExoC3 is widely used in cell biology and is homologous to the exoenzymes EDIN (epidermal differentiation inhibitors) A, B, and C from *Staphylococcus aureus* (*11*) (*12, 13*). These exoenzymes enter host cells via nonspecific endocytic processes and translocate from vesicles into the cytosol. The TEM tunnels form spontaneously upon disruption of actin cytoskeleton-driven contractility controlled by RhoA (*8, 10*). Compressive forces applied to the dorsal region of cells are sufficient to bring apposing membranes into close contact, leading to the opening of TEMs in the presence or absence of EDIN (*14*). The magnitude of the force required to mechanically open TEMs greatly decreases when RhoA activity is inhibited (*14*). Therefore, inhibition of RhoA-driven cytoskeletal tension and depletion of the F-actin meshwork trigger cell spreading and a reduction in cell height, which favour the spontaneous formation of TEM tunnels (*8, 15*). Although TEM tunnels have not yet been visualized in vivo, they form *ex vivo* in the endothelium lining of the inner surface of aortas either infected with *S. aureus*-producing EDIN or treated with purified recombinant EDIN (*8*). The intravenous injection of EDIN or ExoC3 triggers vascular leakage (*8, 16*). Ultimately, cumulative evidence shows that EDIN favours the dissemination of *S. aureus* in host tissues (*17, 18*). Whether genetic factors confer protection to the host against the cytotoxic effects of EDIN-B in septicaemia remains to be determined.

Applying concepts discovered via soft matter physics to cellular microbiology enables us to define mechanical constraints and discriminate purely physical processes from those induced by activated cellular factors (*19, 20*). The phenomenological analogy of TEM tunnel formation and dry patches formed on solid surfaces by viscous liquid dewetting highlights the importance of membrane tension increases in response to cell spreading, which is a critical parameter of TEM tunnel

dynamics (*10*, *21*). Membrane tension participates in TEM nucleation and it controls the initial speed of TEM opening, and tends to be reduced as the TEM is enlarged (*10*, *21*). Despite the theoretical prediction of a key role of membrane tension in TEM opening, the cellular mechano-regulators controlling the TEM opening phase have not yet been identified.

Caveolae are mechano-regulators of the membrane that spontaneously flatten to accommodate acute mechanical loads and thereby prevent membrane rupturing (*22*, *23*). Caveolin complexes, which are essential components in caveolae, insert into the inner leaflet of the lipid bilayer plasma membrane (*23*, *24*). Caveolin-1 homo-oligomers form flat discoid complexes anchored to interfaces (*24*). Membrane bending during caveolar invagination, which form areas 50-100 nm in diameter, requires the cavin-1 structural protein (also referred to as PTRF), which plays an established role with caveolin-1 (*25*–*29*). Membrane invaginations at caveolae are further stabilized by the assembly of a ring of dynamin-like EHD2 oligomers around the caveolar neck (*30*-*32*). In endothelial cells, the cross-talk between caveolin-1 and RhoA during actomyosin contractility leads to critical mechano-sensing of and adaptation to haemodynamic forces (*33*, *34*). Caveolin-1-deficient mice showed an increase in the eNOS signalling critical for RhoA activation via nitration of p190RhoGAP-A, which inactivated its GTPase stimulating activity on RhoA (*35*–*37*). Cell biology and epidemiological studies have recently discovered the importance of caveolin-1 in host–pathogen interactions (*38*–*40*). Considering their critical functions in ensuring membrane mechano-relaxation in response to acute mechanical loads (*22*), caveolae are interesting candidates for the mechano-regulation of TEM tunnels that form upon RhoA inhibition. Together, these findings point to the importance of further characterizing caveolae and the caveolae and caveolin-1 interplay during infection and gaining more information on membrane mechano-regulation.

Here, we report the susceptibility of caveolin-1-deficient mice with septicaemia to the lethal effect of EDIN-B. Our data show that cavin-1-structured caveolae control cell shape parameters, namely, volume and spreading, i.e., the height of cells. The TEM opening speed and theoretical modelling further suggest a role for caveolae in regulating membrane tension. Interestingly, we provide compelling evidence showing that, in contrast to cavin-1 structured caveolae, non-caveolar caveolin-1 contributes to membrane rigidity, accounting for the limitation on maximal TEM width.

## Results

### Loss of caveolin-1 sensitizes mice to EDIN-B lethal effects during *S. aureus* sepsis

No evidence has been reported to show that EDIN factors in *S. aureus* induce lethal effects on mouse models of infection. In this study, we aimed to compare the susceptibility of caveolin-1-deficient mice ($CAV1^{-/-}$) and their wild-type littermates ($CAV1^{+/+}$) to the wild-type *S. aureus* strain LUG1799 (WT *edinB*). LUG1799 belongs to the European lineage ST80 derived from community-acquired methicillin-resistant *S. aureus*, and it expresses the exotoxin EDIN isoform B (EDIN-B) (*18*). We first monitored the mortality of $CAV1^{-/-}$ and $CAV1^{+/+}$ mice challenged with three increasing concentrations of *S. aureus* strain WT *edinB* inoculated through 7 days (Fig. 1A). We did not observe any role for caveolin-1 in mice infected with the predicted nonlethal or lethal inoculum levels. Indeed, all the mice, except one $CAV1^{-/-}$ mouse, recovered from infection induced with $5 \times 10^6$ CFU of bacteria/mouse, and all the $CAV1^{-/-}$ and $CAV1^{+/+}$ mice died 24 hours after intravenous injection of $5 \times 10^8$ CFU of bacteria/mouse. In contrast, when mice were challenged with an intermediate dose of $5 \times 10^7$ CFU/mouse, we found significant differences in susceptibility between $CAV1^{-/-}$ and $CAV1^{+/+}$ mice ($P < 0.001$, Mantel–Cox test). All the $CAV^{-/-}$ mice died on day 1 post-challenge, whereas the death of $CAV1^{+/+}$ mice was delayed between 1 and 2 days, with one $CAV1^{+/+}$ mouse surviving. The loss of caveolin-1 expression thus sensitized the mice to systemic infection by *S. aureus*-produced EDIN-B. We then explained a possible role for EDIN-B in

enhancing CAV1$^{-/-}$ mouse susceptibility to systemic infection. Despite a broad concentration range for the 5 *inocula*, we recorded no difference in the susceptibility of CAV1$^{+/+}$ mice to either the *S. aureus* WT *edinB* or *edinB*-deleted isogenic strain (Δ*edinB*) (Fig. S1). Nevertheless, a lethal dose 50 ($LD_{50}$) of approximately $2.5\times10^7$ CFU/mouse was established for both strains of *S. aureus* (Fig. 1B). Interestingly, when we performed similar experiments with an inoculum of $2.5\times10^7$ CFU/mouse, we found a significant difference in the survival rates of CAV1$^{-/-}$ mice: $n$=11/18 mice infected with *S. aureus* Δ*edinB* versus $n$=4/17 mice infected with *S. aureus* WT ($P$ = 0.0123, Mantel–Cox test) (Fig. 1C). Our study of caveolae-deficient mice reveals the capacity of the EDIN-B exoenzyme to trigger lethal effects in mice via septicaemia.

**Caveolae control the extent of TEM tunnel formation**

The cytotoxic effects of EDIN-like factors include the disruption of RhoA-driven stress fibre and TEM tunnel formation. TEM tunnel formation is triggered by EDIN-like factors and ExoC3 from *C. botulinum*, which is widely used in cell biology studies (Fig. 2A). We first verified that ExoC3 treatment exerted no impact on caveolin-1 and cavin-1 expression in treated HUVECs (Fig. S2A). Importantly, the stoichiometry of caveolin-1 and cavin-1 is highly regulated in endothelial cells (*41*). In this study, we observed that short interfering RNA (siRNA)-mediated depletion of caveolin-1 expression (siCAV1) also led to the estimated reduction in cavin-1 expression by approximately 80%. We also found that the cross-depletion effect triggered by siRNA targeting cavin-1/PTRF (siPRTF) on a cellular pool of caveolin-1 was less pronounced, with an approximate 60% reduction in caveolin-1 signal in cells treated with siPTRF. (Fig. S2B). Similar outcomes obtained with siCAV1 and siPTRF indicated the importance of caveolae structures, and different outcomes indicated specific roles for caveolin-1. We then verified that siRNA-targeted depletion of caveolin-1 and cavin-1/PTRF did not affect the extent of ADP ribosylation of RhoA (Fig. S2C). Ultimately, we verified that TEM tunnels were surrounded by an F-actin bundle after both siCAV1 and siPTRF exposure (Fig. 2A). We then quantified the efficiency of TEM tunnel formation in siCAV1- or siPTRF-treated cells (Fig. 2B). HUVECs were treated with siCTRL, siCAV1 or siPTRF followed by ExoC3. We recorded a higher percentage of cells with TEMs in the population of caveolae-deficient cells: 37.6% (s.d. of 1.3%) in the siCAV1-treatment condition, 36.4% (s.d. of 1.3%) in the siPTRF-treatment, compared to 28.8% (s.d. of 1.2%) in the siCTRL group (Fig. 2B). Moreover, we observed a significant increase in the density of TEM tunnels per cell in both the siCAV1 ($N_{TEM\_siCAV1}$ = 1.96) and siPTRF ($N_{TEM\_siPTRF}$ = 1.36) groups, compared to that of the siCTRL ($N_{siCTRL}$ = 0.91) group (Fig. S3A). Increases in TEM tunnel density per cell and within the cell population were similar when cells were treated with EDIN but not ExoC3 (Fig. S3B-C). To further determine the importance of caveolae in counteracting TEM tunnel formation, we depleted the caveolae-stabilizing protein EHD2 in cells. The depletion of EDH2 in siEHD2-treated cells did not affect the cellular levels of caveolin-1 and cavin-1 (Fig. S4A). An analysis of the population of EHD2-depleted cells revealed an increase in TEM tunnel formation as well as an increase in the density of TEMs per cell (Fig. S4B and S3C). These data show that caveolin-1, cavin-1, and EHD2 hence fully assembled caveolae limit the formation of TEMs in the cell population.

**Caveolae control the cell shape parameters of volume and spreading**

Reduction in cell height once RhoA signalling is inhibited favours the fusion of apposing plasma membranes, creating TEM nucleation sites (*14*, *15*). The height of cells is proportional to the volume divided by the cell spreading area. Hence, we investigated the role played by RhoA, caveolin-1 and cavin-1 in the extent of cell spreading and associated volume variations. The spreading area was estimated from the measurement of cell perimeters (Fig. 3A). The volume of cells was quantified via fluorescent dye exclusion, as depicted in Fig. 3B and as previously described in (*42*). Upon cell treatment with siCTRL, we recorded a significant increase, of 17%, in the spreading area and cell volume (Fig. 3C-D, Table 1). Nevertheless, alterations to cell shape

resulted in a 15% decrease in cell height (Table 1). When siCAV1- and siPTRF-treated cells were treated with ExoC3, we recorded an increase in the spreading area of cells, and this effect was associated with a reduction in the volume of the cells (Fig. 3C-D). Thus, ExoC3 treatment induced a 20% reduction in cell height after siCAV1 treatment and a 24% reduction after siPTRF treatment compared to height in the siCTRL-treated cells (Table 1). The magnitude of the cell height reduction was in good agreement with our findings showing that siCAV1 and siPTRF treatments promoted TEM formation to a similar extent. There was a noticeably stronger regulatory effect of siPTRF treatment compared to that of siCAV1 treatment on cell shape parameters, further indicating the key role of caveolae in the control of the cell shape parameters of volume and spreading (Fig. 3C-D). In conclusion, the disruption of caveolae in ExoC3-treated cells produced a concomitant decrease in cell volume and an increase in cell spreading.

**Caveolae and F-actin distribution at the plasma membrane**

Although the crosstalk between RhoA and caveolae controls endothelial cell adaptation to mechanical load, we lack information on whether inhibition of RhoA modulates the density of caveolae invaginations at the endothelial cell plasma membrane. We implemented a well-established unroofing approach to expose the plasma membrane and directly visualize caveolae on a platinum replica via transmission electron microscopy (*43*). In both naïve and ExoC3-treated cells, we observed membrane-associated cytoskeleton filaments, the honeycomb structure of clathrin sheets, clathrin-coated pits, and rough aspects of pits similar to caveolar invaginations (Fig. 4A). However, the density of the cytoskeletal filaments was less pronounced in the ExoC3-treated cells. Cells were then transfected with a plasmid encoding GFP-caveolin-1 to confirm the presence of caveolin-1 in caveolae invaginations by GFP-immunogold labelling (Fig. 4B). Notably, we did not observe a detectable accumulation of caveolae around TEM tunnels. We quantified the density of caveolae in control and ExoC3-treated cells. In total, we analysed an area $A_{area} > 175\ \mu m^2$ under each condition ($n \geq 16$ membrane areas of independent cells per condition). We found a 1.6-fold decrease in the mean density of caveolae in the ExoC3-treated cells, which exhibited 3.4 caveolae/$\mu m^2$ of membrane (s.d. of 2.1 caveolae/$\mu m^2$), compared with 5.4 caveolae/$\mu m^2$ of membrane (s.d. of 3.1 caveolae/$\mu m^2$) in untreated control cells (Fig. 4C). Since RhoA-mediated formation of a cytoskeleton tensile meshwork counteracts the formation of TEM tunnels, we performed 2D stochastic optical reconstruction microscopy (STORM) imaging, which revealed a thin F-actin meshwork with ~30-nm resolution. Fig. 4D depicts examples of the high density F-actin meshwork that formed between well-defined thick actin cables in untreated HUVECs. In contrast, after siRNA treatment, the cells treated with ExoC3 showed profound reorganization of the actin cytoskeleton, which formed a loose meshwork of thin actin filaments and bundles intercalated with large zones devoid of F-actin. We found significant widening of the F-actin network mesh in ExoC3-treated cells (Fig. 4E). Altogether, cells treated with ExoC3 displayed caveolae invaginations at the membrane and a loosened actin filament mesh.

**Different impacts of cavin-1 and caveolin-1 on TEM tunnel formation dynamics**

Given the large transcellular apertures formed, the density, diameter and lifetime of TEM tunnels are thought to be critical in the control of endothelial permeability. To quantify the effects of caveolae and describe them in a biophysical model of their functions, we implemented a pipeline of live-cell imaging and semiautomatic measurements of TEM opening speed and TEM maximal width (*15*). This method relied on the detection of the Lifeact-GFP signal at the edge of TEM tunnels and postprocessing of variations in TEM tunnel width as a function of time (*15*). After we performed this analysis, we projected the surfaces of all the TEM tunnels that had formed over a 1-hour period of recording when they first opened onto the image showing the Lifeact-GFP signal

(Fig. 5A). Thus, we established that a TEM opened preferentially at the cell periphery where the cell height was minimal and that TEMs showed negligible overlap (Fig. 5A). Notably, we observed wider TEMs in siCAV1-treated cells than in the siPTRF- and siCTRL- treated cells (Fig. 5A). A quantitative analysis established a 5.4-fold increase in the maximal TEM formation area under caveolin-1-depleted conditions compared to that under siPTRF and siCTRL conditions (Fig. 5B). The widening of TEMs in siCAV1 was observed within the same time frames in which TEM opening was initiated ($t_{max}$): $t_{max\_siCTRL}$=1.4 min (s.d. of 2.3 min.), $t_{max\_siCAV1}$=1.3 minutes (s.d. of 1.3 min) and $t_{max\_siPTRF}$=1.2 min (s.d. of 1.4 min.). In addition, overall similarities in TEM tunnel formation cycles were observed between 13 and 16 min (Fig. 5C). Altogether, these findings point to caveolin-1 as a key regulator of the opening speed and widening of TEMs (Fig. 5C). According to the dewetting theory as applied to TEM opening, the impact of membrane tension was maximal at the onset of TEM opening (see the physical model description in the Materials and Methods). This finding prompted us to obtain a second series of live-cell imaging at a 10-fold higher temporal resolution to resolve the TEM opening speed ($S_o$). In good agreement with our aforementioned data, we recorded no significant variation in the TEM opening speed between the siCTRL- and siPTRF-treated groups (Fig. 5D). In contrast, we recorded a 2-fold higher TEM opening speed in caveolin-1-depleted cells $S_{o\_siCAV1}$=2.4 $\mu m^2/s$ versus $S_{o\_siCTRL}$=1.1 $\mu m^2/s$ (Fig. 5D). Thus, caveolin-1 specifically controls the TEM opening speed and maximal width.

We next inferred changes in membrane mechanical properties due to the depletion of caveolin-1 or cavin-1 using a refined theoretical model of cellular dewetting. This model accounts for the presence of several TEMs opening simultaneously (see the physical model description in the Materials and Methods). Importantly, the model is based on the hypothesis that plasma membrane deformation enabling TEM nucleation and tunnel growth is a function of membrane tension and bending rigidity, within the limit of an absence of contribution of membrane adhesion to cortical cytoskeleton (*44*). Indeed, consistent with a minimal impact of cortical cytoskeleton elements on membrane mechanics, the data recorded via 2D STORM established the disassembly of the F-actin meshwork in ExoC3-treated cells (Fig. 4D). As explained in the Materials and Methods section in detail, the model predicts that the initial opening speed is proportional to the membrane tension, consistent with a critical role of membrane tension in TEM growth (*9*). From this, the model predicted a significant 2-fold increase in membrane tension in cells treated with siCAV1, and no effect in siPTRF-treated cells. The model also predicted a maximum TEM size that greatly depended on membrane bending rigidity but weakly on initial membrane tension. Thus, by fitting the observed maximum TEM sizes observed under different treatment conditions, the model provided an estimate of the variation in bending rigidity. Using values obtained from the siCTRL-treated cells, which were a $\sigma_0$ = 2.5 $10^{-5}$ N/m for the initial membrane tension (45) and $\kappa$ = 23.4 $k_BT$ for the bending rigidity (direct measurement, see below), the model predicts a 15% reduction in membrane bending rigidity upon silencing of cavin-1 expression; and a 55% reduction after caveolin-1 depletion (Fig. 5D). In conclusion, the physical model points to the dominant function of caveolin-1 in controlling membrane tension and bending rigidity, which stands in contrast with the marginal or negligible effect predicted for cavin-1.

**Differential impacts of caveolin-1 and cavin-1 on membrane rigidity**

Our study of TEM dynamics suggests that caveolin-1 controls membrane mechanical parameters, particularly bending rigidity. Therefore, this parameter was further investigated using a quantitative method based on pulling membrane tethers from cell-derived plasma membrane spheres (PMSs) (*22*, *46*, *47*) (Fig. 6A). The use of PMSs allowed us to study the mechanical properties of the plasma membrane without the F-actin cortex (*47*). PMSs prepared from untreated siCTRL-, siCAV1-treated and siPTRF-treated HUVECs were aspirated into a micropipette, allowing to control the membrane tension by changing the aspiration pressure. Membrane tethers were pulled from PMSs

using optical tweezers which can be used to measure the force, *f*, exerted on the membrane tether at given values of membrane tension (*46*) (Fig. 6B-C). The following equation shows the scale of *f* in relation to the square root of the bending rigidity ($\kappa$) and membrane tension ($\sigma$):

$$f = 2\pi\sqrt{2\kappa\sigma}$$

(*48*); thus, an analysis of the slope of the square of the force as a function of membrane tension provides a measurement of the membrane bending rigidity of a PMS (Fig. 6D). We measured a significant decrease of 30% of the bending rigidity from $\kappa$ = 23.4 $k_BT$ (s.d. of 0.9 $k_BT$) in siCTRL conditions to $\kappa$ = 17 $k_BT$ (s.d. of 0.9 $k_BT$) in siCAV1 conditions. Moreover, we observed no significant difference in bending rigidity in siPTRF conditions compared with siCTRL conditions, with a $\kappa$ of 23.4 $k_BT$ (s.d. of 1.3 $k_BT$) (Fig. 6D). In agreement with the analysis deduced from our dewetting model, these measurements reveal an intrinsic property of non-caveolar caveolin-1 in the control of plasma membrane rigidity.

## Discussion

We reported the protective function of caveolae against the lethal effect of EDIN-B obtained from *S. aureus* in mice with septicaemia. Moreover, the cellular depletion of caveolin-1 and cavin-1, which are essential components of caveolae, as well as the depletion of the ATPase EHD2, an accessory protein, sensitized endothelial cells to the formation of TEM tunnels. We established a specific role for caveolin-1 in controlling the initial opening speed and maximal width of TEMs. These data, framed in the theoretical model of dewetting, led us to infer that caveolin-1 contribute to membrane rigidity. Moreover, we reported fine-tuning of cell shape by cavin-1-structured caveolae in response to a decrease in RhoA-driven actomyosin contractility. Cell shape changes included a decrease of cell volume and an increase of spreading area. Together these effects decreased the height of the cells and likely favoured the contact of plasma membranes, creating TEM nucleation sites. In summary, this work establishes new distinct functions for caveolin-1 and cavin-1-structured caveoale in the regulation of membrane rigidity and cell shape, respectively.

Considering the analysis of variations in the width of the TEMs using the cellular dewetting model, we provided compelling evidence that caveolin-1 controls not only the parameters related to membrane tension but also those related to membrane bending rigidity. This was independently supported by conducting membrane-tether-pulling experiments using plasma membrane spheres, where we found that depletion of caveolin-1 decreased membrane rigidity by 30%, whereas cavin-1 depletion exerted no effect. The differences between analysis of the TEM opening dynamics with the model that provided a 55% decrease and biophysical measurements can be attributed to several simplifications used in the theoretical model, notably the simplified treatment of physical membrane tension variation, cytoskeletal contributions, and interactions between neighbouring TEM tunnels. The mechanical role played by caveolin-1 is of profound significance considering that the inclusion of integral proteins into membranes had no impact on bending rigidity of membranes, as has been reported on the basis of cylindrical bacteriorhodopsin experiments (*49*), and the inclusion of integral proteins may even decrease membrane stiffness, as reported for the conical $Ca^{2+}$-ATPase SERCA (*50*). Previously performed simulations also confirmed the softening effect of protein inclusions on membrane shape (*51*). Nevertheless, our observations can be explained by a high density of rigidity-promoting inclusions of the plasma membrane (>>10%), which was generally not achievable with the reconstituted membranes described in the aforementioned references.

Caveolin-1 may contribute to plasma membrane rigidification through numerous effects, i.e., by structuring ordered lipid domains or anchoring the membrane to cortical cytoskeletal components. Considering this last point, disruption of the interactions between the plasma membrane and the cell cortex after caveolin-1 depletion is expected to exert little effect upon RhoA inhibition. This supposition was supported by our STORM images showing dramatic disassembly

of the F-actin meshwork in ExoC3-treated cells. Furthermore, the low contribution of cortex–membrane interactions to membrane mechanics in treated cells was in good agreement with the decrease in Young's modulus of the cell cortex in ExoC3-treated cells (*14*), pointing to dominant roles for membrane intrinsic mechanical parameters when RhoA is inactivated. Moreover, previous studies have established that caveolae in the membrane are enriched with cholesterol, sphingomyelin, and glycosphingolipids, including gangliosides (*52, 53*), which are known to rigidify membranes (*54*). Thus, caveolin-1 might contribute to the enrichment of the plasma membrane with these lipid species. We did not establish experimental conditions allowing us to deplete cholesterol without compromising the shape of HUVECs, which precluded proper analysis of TEM dynamics. Moreover, a previous attempt to increase the width of TEMs by softening the membrane through the incorporation of poly-unsaturated acyl chains in phospholipids failed, likely due to the homeostatic adaptation of membrane mechanical properties (*15*). Further studies are required to establish whether and how caveolin-1 oligomers (*24*) can control membrane mechanical parameters.

Our data point towards a major effect of cavin-1 in regulating the spreading area and the volume of cells, which might be linked to cavin-1 driving caveolae invaginations. Our data showed that ExoC3 treatment induced an increase in cell volume, and cell spreading was enhanced. With siCAV1-treated cells, similar effects were observed but only after ExoC3 treatment. The uncoupling of cell spreading and volume decrease could be due to the known permissive effect of RhoA signalling; this swelling could induce the establishment of an outwardly rectifying anion current mediated via the volume-rectifying anion channels (*55, 56*). Interestingly, a decrease in cell volume identified upon depletion of cavin-1, and to a lesser extent after caveolin-1 depletion, was an outcome independent of RhoA signalling. How caveolae control cell volume in treated cells awaits determination. Our findings suggest that depletion of caveolae, as well as the inactivation of RhoA, may release membrane-folding mechanical constraints that limit cell spreading. Another hypothesis is that caveolae control cell shape parameters through cavin-1 regulation of cell signalling (*57–60*).

The molecular basis of interindividual variability after infection with *S. aureus* is unclear (*39*). Here, we established that the loss of caveolin-1 expression sensitized animals to deadly effects triggered by EDIN-B during *S. aureus* septicaemia. Although we cannot argue for a causal link between the lethal effect of EDIN-B in caveolin-1-deficient animals and the protective function of caveolin-1 against TEM tunnel formation in endothelial cells, these findings represent a first step towards establishing that endothelial cells regulate TEM tunnel formation and width in vivo; this hypothesis is supported by previous findings showing that inhibition of RhoA reduces paracellular permeability, increasing transcellular permeability, and that ADP-ribosyltransferases targeting RhoA increase vascular permeability to induce animal death after TEM opening is no longer controlled (*8, 16*). Consistent with the role played by caveolin-1 in infection, analysis of an observational cohort of patients with *S. aureus* community-acquired pneumonia indicated that EDIN-B, together with Panton–Valentin leukocydin, is positively associated with the haemoptysis aetiology, which manifests as blood in sputum (*61*). In line with this finding, a previous study suggested that EDIN-B might promote the translocation of *S. aureus* from lung tissues to the bloodstream (*18*). Recently, a human genetics study pinpointed the impact of haploinsufficiency of the OTULIN deubiquitinase in sensitizing host cells to lysis triggered by the highly prevalent α-haemolysin pore-forming toxin of *S. aureus*, a major determinant in staphylococcal pneumonia (*39*). Patients with a deleterious OTULIN allele suffer life-threatening skin disease and pulmonary necrosis typically triggered by *S. aureus* infection. Defects in OTULIN activity lead to an increase in caveolin-1 cellular protein levels in dermal cells, which in turn upregulates the expression of ADAM10, which encodes a host cell surface receptor of an alpha-haemolysin pore-forming toxin.

Collectively, our findings ascribe caveolin-1 expression level variations to key functions in *S. aureus* infection.

## Materials and Methods

### Bacterial strains and culture conditions

*S. aureus* HT20020209-LUG1799, referred to as wild-type WT *edinB* in this study, is a minimally passaged ST80 *SCCmecIV* PVL+ MRSA strain isolated in France (deposited at http://www.ebi.ac.uk/ena) that is representative of ST80 CA-MRSA clones (*62*, *63*). *S. aureus* HT20020209-LUG1799 with the *edinB* gene deletion is referred to as Δ*edinB* in this study (*18*). Both strains were grown in lysogeny broth (LB) with shaking at 200 rpm and 37 °C. Equal growth kinetics were verified (not shown).

### Mouse infection model

Adult male and female B6.Cg-*Cav1*$^{tm1Mls}$/J mice (strain #: 007083, Jackson Laboratories) and C57BL/6J mice (Charles River) were housed under specific-pathogen-free conditions at the Institut Pasteur animal facilities licenced by the French Ministry of Agriculture (B75150102). Mice received food and water ad libitum, and their weight was recorded daily throughout the study. *S. aureus* strains were cultured in LB at 37 °C until reaching an $OD_{600}$ = 1 after overnight culture. After washing twice in PBS, cell pellets were resuspended in sterile 0.9% NaCl. Infections were carried out by injecting 300 µL serial dilutions of inoculum intravenously into the tail vein of the mice. Animal survival was monitored daily.

### Ethics statement.

Animal experiments were performed according to Directive 2010/63/EU of the European Parliament and conformed to the European Council Directive on the approximation of laws, regulations, and administrative provisions of the Member States regarding the protection of animals used for experimental and other scientific purposes (86/609/EEC). The experimental procedures were approved by the Animal Experimentation Ethics Committee and the Risk Prevention Service of the Institut Pasteur (approval numbers 210119 and N° 21.264) and authorized by the French Ministry of Higher Education, Research and Innovation (APAFIS #34712-2022011814537622 v2).

### Cell culture, transfection and toxicity

Primary human umbilical vein endothelial cells (HUVECs, PromoCell) were cultured in human endothelial serum-free medium (SFM, Gibco) containing 20% foetal bovine serum, 20 ng/ml FGF-2, 10 ng/ml EGF, and 1 µg/ml heparin and referred to as complete SFM (SFMc). Cells were cultured on gelatine-coated culture ware at 37 °C with 5% $CO_2$ for as many as six passages. For siRNA transfection, HUVECs were cultured at a density of 38,000 cells/cm$^2$. ON-TARGETplus smart pool siRNA (Dharmacon) targeting human caveolin-1 (L-003467-00-0005), EHD2 (L-016660-00-0005), cavin-1/PTRF (L-012807-02-0005) or control RNAi SR-CL000 (Eurogentec) was used at 100 nM via magnetofection technology (OZ Biosciences) following the manufacturer's instructions in serum-free OptiMEM (Gibco). When necessary, cells were electroporated 24 h post-magnetofection and then used from 48 to 54 h post-magnetofection. HUVEC electroporation of plasmids encoding caveolin-1-GFP (*22*) or Lifeact-GFP (Ibidi, GmbH, Planegg/Martinsried, Germany) was performed as described in (*64*). Briefly, cells were trypsinized and resuspended in Ingenio Solution (Mirus) containing plasmid DNA (10 µg/$10^6$ cells) in a 4-mm cuvette (CellProjects). Cells were then electroporated at 300 V and 450 µF with one pulse of a GenePulser

electroporator (Bio–Rad). Cells were incubated in SFMc, and the medium was replaced 3 h post-electroporation. Cells were treated 6 h post-electroporation. Recombinant ExoC3 and EDIN were produced in *E. coli* and purified as described in (*8*). Cells were treated with ExoC3 or EDIN toxin at a final concentration of 100 µM for 24 h.

**Immunoblotting and Western blotting**

Proteins were resolved on 12% SDS-polyacrylamide gels and transferred to nitrocellulose membranes (GE Healthcare). The primary antibodies used were mouse anti-EHD2 (L-05) (Santa Cruz sc-100724), rabbit anti-Cav1 (Cell Signaling Technology #3238), rabbit anti-PTRF (Proteintech, 18892-1-AP) and mouse anti-GAPDH (Santa Cruz sc-47724). The secondary antibodies used were HRP-conjugated anti-mouse or anti-rabbit (Dako). Signals were imaged using a Fujifilm LAS-3000 system and quantified with ImageJ software.

**Immunofluorescence**

HUVECs were seeded on a gelatine-coated µ-Dish 35 mm, high (Ibidi) and treated as indicated previously (*65*). Cells were fixed in ready-to-use paraformaldehyde, 4% in PBS (Bio–Rad). Immunostaining of fixed cells permeabilized in 0.5% Triton X-100 was performed. FITC-phalloidin or TRITC-phalloidin at 1 µg/ml (Sigma) were used to stain actin, and DAPI (Life Technologies) was used to label nuclei.

**Video microscopy**

HUVECs were electroporated with LifeAct-GFP-pCMV as described above and seeded on a gelatine-coated polymer coverslip dish (Ibidi). After treatment with the toxins (see above), the cells were supplemented with 25 mM HEPES (pH 7.4) and their proliferation was recorded at 37 °C with a Nikon T*i* inverted microscope using an Ultraview spinning disk confocal system (Perkin Elmer). For determining TEM opening, images were taken every 10 seconds for 1 h. To determine the opening speed ($S_o$), images were taken every second for 30 min. Acquired videos were analysed via an ICY-based semiautomatic protocol.

**Cell volume measurement**

After siRNA treatment and other treatments, cells were seeded onto a PDMS chip ($2.10^6$ cells/mL) as described previously (*42*). Briefly, chambers were coated with 10 µg/ml fibronectin in PBS (Life Technologies) for 1 h at RT. Chambers were washed with medium before cell seeding. Cells were resuspended in medium supplemented with 0.5 mg/ml Alexa Fluor 488 dextran (MW 10 kD; Life Technologies) and then injected into the chamber. Finally, the chamber was immersed in medium to prevent evaporation. HUVECs were allowed to adhere for 4 to 6 h in SFMc at 37 °C with 5% $CO_2$ before acquisition.

Images were analysed with MATLAB (MathWorks). The intensity of the background was maximal in the absence of any object ($I_{max}$) and represented the fluorescence value for the maximal height of the chamber ($h_{max}$). In contrast, the pillar excludes fluorescence, which therefore reflects the minimal fluorescence intensity ($I_{min}$). At the cell level, the fluorescence was partially excluded at a given point for a cell at a given height ($h_{x,y}$). This strategy enables the measurement of the fluorescence intensity at this point ($I_{x,y}$). After calibrating the fluorescence intensity signal $\alpha = (I_{max} - I_{min})/h_{max}$, integration of the fluorescence intensity over the cell area provided the cell volume ($V_{cell}$):

$$V_{cell} = \iint_{x,y} \frac{Imax - Ix,y}{\alpha} dxdy$$

**Metal replicates and transmission electron microscopy**

Metal replicates of the ventral plasma membranes of HUVECs cultured on glass coverslips were obtained by sonication according to a published protocol (Heuser 2000b) and adapted by S. Vassilopoulos, our collaborator. Briefly, cells were rinsed three times with Ringer's buffer with $Ca^{2+}$ and then briefly subjected to a concentration of 0.5 mg/mL poly-L-lysine diluted in $Ca^{2+}$-free Ringer's buffer (Sigma–Aldrich). Poly-L-lysine was removed by washing with $Ca^{2+}$-free Ringer's buffer. The coverslips were immersed in KHMgE buffer at 37 °C before sonication (Vibra-Cell VCX130 ultrasonic processor, Sonics) at a 20% amplitude. The unroofed cell membranes were then immediately fixed for 30 minutes with 2% glutaraldehyde/2% paraformaldehyde (PFA). The cell membranes were sequentially treated with 1% OsO4, 1.5% tannic acid and 1% uranyl acetate before dehydration via successive ethanol baths, which was ultimately substituted with hexamethyldisilazane (HMDS) (#C16700-250; LFG Distribution).

For immunogold labelling, sonicated plasma membranes were fixed with 4% PFA before incubation with primary (GFP Thermo Fisher A11122 Rabbit 1/20) and secondary antibodies coupled to gold beads (rabbit-gold 815.011 AURION goat 1/25), and the membranes were then incubated with a $NaBH_4$ solution to inactivate aldehydes. The membranes were finally fixed with 2% glutaraldehyde and subjected to the same treatment as that used for morphology studies. The dehydrated samples were metalized via rotary metallization. The coverslips were placed in the chamber of a metallizer (ACE600, Leica Microsystems). Once under a high vacuum ($>10^{-5}$ mBar), the membranes were covered with 2 nm of platinum stabilized by 4 to 6 nm of braided carbon. The resulting platinum replicas were separated from the glass by flotation on acid, washed several times in distilled water baths containing 0.1% detergent (one drop in 10 mL, Photo-Flo, Kodak), and placed on electron microscopy (EM) grids covered with a carbon film (200 mesh formvar/carbon, LFG Distribution). The grids were mounted in the goniometer with eucentric side entry of a transmission electron microscope operating at 80 kV (CM120, Philips), and images were recorded with a Morada digital camera (Olympus). The images were processed by ImageJ software to adjust brightness and contrast and are presented in reverse contrast.

**RhoA ADP-ribosylation assay**

HUVECs were seeded at a density of 27,000 cells/$cm^2$ transfected with siCTRL, siCAV1 and siPTRF and then treated with or without ExoC3. Cells were lysed in ADP-ribosylation buffer (20 mM Tris-HCl, 1 mM EDTA, 1 mM DTT, 5 mM $MgCl_2$ and cOmplete protease inhibitor EDTA-free (Roche), pH 7.5) and passed through a 27G syringe 20 times. Cell lysates were collected by centrifugation at 12,000 g for 10 min, and the protein concentration was determined by BCA assay (Thermo Fisher Scientific). The reaction was carried out by incubating 20 µg of cell lysate with 2 µg ofExoC3 and 10 µM 6-biotin-17-$NAD^+$ (BioLog) at 37 °C for 30 min. The reaction was terminated by the addition of 1 mM DTT and Laemmli buffer (0.3 M Tris-HCl, 10% SDS, 37.5% glycerol and 0.4 mM bromophenol blue) and boiling at 100 °C for 5 min. The samples were subjected to 12% SDS–PAGE, and the proportion of ADP-ribosylated (i.e., biotin-ADPr-RhoA) RhoA in the sample was measured by Western blotting using streptavidin–peroxidase.

**Plasma membrane sphere formation and tether extraction**

Plasma membrane spheres (PMS) were generated via a protocol adapted from (*47*). Cells were grown to 60–80% confluence on gelatine-coated 100-mm dishes and incubated for 6–8 h in PMS buffer [1.5 mM $CaCl_2$, 1.5 mM $MgCl_2$, 5 mM HEPES, 2 mg/ml glucose, 150 mM NaCl, 10 µM MG132 in PBS (pH 7.4)] to induce membrane swelling of the PMSs. Individual PMSs were aspirated using a casein-passivated micropipette connected to a piezo-stage (PI, Karlsruhe, Germany) for manipulation and to a hydrostatic aspiration control system (*66*). Micropipettes were made in house with borosilicate capillaries pulled into fine cones using a laser pipette puller (P-2000, Sutter Instrument Co.) and microforged at the desired inner diameter (3-4 µm) as described previously (*22*). For the extraction of tethers from PMSs, we used optical tweezers built in-house

that consisted of a single fixed laser beam (infrared laser wavelength of 1070 nm) focused through a 60X water objective mounted on a confocal microscope (Nikon TE2000 inverted microscope) (*67*). To pull tethers from PMSs, we coated streptavidin beads (3 µm in diameter, Spherotech) with fibronectin, which allowed the beads to bind to PMSs. A membrane tether was generated by bringing the micropipette-held PMS into contact with a bead trapped by the optical tweezers, and then by moving the PMS away from the bead. After extraction, the tether was held at a constant length between 2 and 5 µm, and tether forces were measured during gradual increase in aspiration pressure and thus PMS tension. At a given membrane tension, the corresponding tether force was measured at least 30 s after the pressure change and when equilibration was established. Analysis was performed as described below. Briefly, for each membrane tether, the tether force ($f$) was plotted as a function of the square root of the membrane tension ($\sqrt{\sigma}$) calculated using the Laplace law (*68*) and corrected when the length of the "tongue" of a PMS tether inside the micropipette was shorter than the radius of the pipette (*69*). For each tether, we determined a force $f_0$ corresponding to the intercept of the linear regression ($f$ vs. $\sqrt{\sigma}$). To estimate the bending rigidity for PMSs obtained from membranes of cell treated differently (siCRTL, siCAV1 and siPTRF cells), the data obtained for all tethers were pooled and rescaled as $(f-f_0)^2/8\pi^2$ and plotted as a function of membrane tension. The corresponding PMS rigidity was obtained from the slope of the linear fit.

**Single-Molecule Localization Microscopy of F-actin**

For single-molecule localization microscopy (SMLM) of F-actin, we used 2D STORM. HUVECs were cultured on 1.5 high-performance coverslips coated with 10 µg/mL fibronectin for 2 h at room temperature. Soluble G-actin was pre-extracted (0.25% Triton, 0.1% glutaraldehyde in 80 mM PIPES, 5 mM EGTA, and 2 mM $MgCl_2$, pH 6.8) for 30 s at 37 °C. The cells were then treated with glutaraldehyde (0.25% Triton, 0.5% glutaraldehyde in 80 mM PIPES, 5 mM EGTA, 2 mM $MgCl_2$, pH 6.8) for 10 min at 37 °C. Glutaraldehyde was quenched for 7 min at RT (0.1% $NaBH_4$ in PBS). Saturation was reached after 1 h at RT (0.22% gelatine and 0.1% Triton X-100 in PBS, pH 7.3). Actin filaments were stained overnight at 4 °C with phalloidin-AF647 (500 nM in PBS). Cells were then placed in switching buffer freshly prepared before imaging [50 mM Tris, 10 mM NaCl, 10% glucose, 0.5 mg/mL glucose oxidase, 50 µg/mL catalase, and 50-100 mM cysteamine (MEA, pH 8.3)] in the presence of phalloidin A647 (10-50 nM). Super-resolved images were acquired with an Elyra-7 SMLM microscope (Carl Zeiss, Germany) using a na=1.4 oil 63x objective (Carl Zeiss, Germany) with 1.518 refractive index oil (Carl Zeiss, Germany) and a pco.edge 4.2 camera system (Excelitas PCO GmbH). All processing analyses were performed with Zen software (Carl Zeiss, Germany). Localization of individual molecules was determined using a peak mask size of 15-pixel diameter and a peak intensity-to-noise ratio between 5 and 6. Drift was corrected using a model-based algorithm from Zen software. Super-resolution images were reconstructed at a 20-nm pixel size.

**Mesh analysis of the F-actin network imaged via 2D STORM**

To quantify actin mesh size from the superresolution images, we developed an image analysis workflow to reliably segment the delimiting continuous actin filaments. First, we clipped the images to a maximum detection count of 10 and applied a line enhancement filter to suppress short apparent discontinuities by modifying a previously described approach (*70*). Specifically, the maxima of the mean intensities along line profiles at 15 equally spaced orientations around each pixel were calculated (line length 21 px or approximately 0.4 µm). Subsequently, tube-like structures were extracted from the line-enhanced images by applying a Hessian filter implemented in scikit-image (smoothing width of 2 px) as described previously (*71*) and binarising the result using Otsu thresholding. The obtained masks were subdivided into putative filament segments by defining sections of equal length along the mask's morphological skeleton and assigning each pixel

to its nearest segment (the chosen length was 20 px or approximately 0.4 μm). The final actin filament segmentation was performed considering only segments that: 1) were not morphologically connected to at least one other segment, to exclude non-filament detections, or 2) exhibited a mean detection count lower than the super-resolution image Otsu threshold. Finally, the actin meshwork was obtained as the connected components of the inverted actin filament segmentation mask.

**Physical modelling**

TEM dynamics were theoretically interpreted on the basis of the generalization of our earlier model, which was used for a single TEM (*21*, *65*), to account for the case when several TEMs open simultaneously. This generalization was previously used to interpret the data in (*15*), and we present it here for completeness. The opening of a TEM is driven by a net force,

$$F_d = 2\sigma - \frac{T}{R}, \tag{1}$$

where σ is the membrane tension, $T$ is the line tension, and $R$ is the TEM radius. For a model lipid membrane in the entropic regime, membrane tension $\sigma$ depends on $R$, quantified by the Helfrich's law. Written in a generalized form to describe $N$ simultaneous TEMs in the same cell, Helfrich's law states that:

$$\sigma = \sigma_0 \exp\left[-\frac{\sum_{i=1}^{N} {R_i}^2}{R_c^2}\right] \tag{2}$$

where $R_c^2 = \left(R_{cell}^2 k_B \hat{T}\right)/(8\pi\kappa)$, $R_{cell}$ is the radius of the cell, $k_B$ is the Boltzmann constant, $\hat{T}$ is the temperature, and $\kappa$ is the effective bending rigidity of the cell membrane. While rigorously derived for a pure lipid membrane, we assumed that Helfrich's law is applicable to describe the relationship between the effective membrane tension $\sigma$ acting on TEMs and the observed projected surface in our cells. Thus, the parameter $\kappa$ in Eq. 2 is an *effective* bending rigidity that accounts for the role played by protein inclusions and the mechanical contribution of the remaining cytoskeletal elements after cell treatment with the toxin. Moreover, we assumed that an eventual buffering role played by the remaining caveolae can be described through modification of the effective parameters $\sigma_0$ and $\kappa$.

As discussed by (*21*), the effective line tension is not a constant; it increases with time due to the formation of an actomyosin cable around the TEM. Stefani et al. described this increase as linear, $T \sim \alpha t$. The dynamics of TEM opening are derived from a balance between the driving force (Eq. 2) and cell–substrate friction. Assuming $N$ identical TEMs, this balance is

$$2\sigma_0 R \exp\left(-\frac{NR^2}{R_c^2}\right) - \alpha t = \mu R^2 \frac{dR}{dt}, \tag{3}$$

where $\mu$ is the friction coefficient. While this equation can be solved numerically, the following analytical approximation can also be obtained, as derived in (*15*):

$$x \exp x^2 \approx \frac{8\,\sigma_0^2\sqrt{N}}{\mu\,\alpha\,R_c}, \tag{4}$$

where $x = N^{1/2} R_{max}/R_c$ and $R_{max}$ are the maximum TEM radii. As discussed in (*15*), for biologically relevant values of the model parameters, Eq. 4 leads to the following approximate estimate of the effective membrane bending rigidity:

$$\kappa \approx \frac{k_B \hat{T}}{8\pi} \frac{A_{\text{cell}}}{N\,A_{max}}. \tag{5}$$

Considering the experimental results shown in Table 2 and using the estimate $\kappa \sim (N \cdot A_{max})^{-1}$ based on Eq. 5, we deduced an effective bending rigidity after silencing cavin-1/PTRF. These

approximate estimates can be refined using Eq. 4 directly, which also takes into account variations in membrane tension. The following expression for the bending rigidity is thus obtained:

$$\kappa \approx \frac{k_B \hat{T}}{8\pi} \frac{R_{\mathrm{cell}}^2}{N R_{\mathrm{max}}^2} \ln\left(\frac{8\,\sigma_0^2}{\mu\,\alpha\,R_{\mathrm{max}}}\right). \quad (6)$$

Eq. 6 is used to obtain the predictions of bending rigidity variations mentioned in the text: a reduction in effective bending rigidity by a factor of approximately 1.2 for siPTRF cell membranes and by a factor of approximately 2.3 for siCAV1 cell membranes, which is equivalent to a 15% decrease for siPTRF and 55% for siCAV1 cell membranes.

*Fit of the initial opening speed*

For short time intervals, the differential equation for the opening dynamics can be simplified to

$$\mu R^2 \frac{dR}{dt} = 2\sigma_0 \left(1 - \frac{R_n}{R}\right), \quad (7)$$

where $R_n = T/(2\sigma_0)$ is the minimal nucleation radius. This equation can be integrated to obtain

$$R_n^2 \ln\left(\frac{R}{R_n} - 1\right) + R_n R + \frac{R^2}{2} - C = \frac{2\sigma_0}{\mu} t\,, \quad (8)$$

where $C$ is an integration constant, whose value is such that $R = R_0$ for $t = 0$, with $R_0$ the unknown nucleated TEM radius, which is larger than the minimal nucleation radius $R_n$; $R_0 > R_n$. Because all TEM measurements are reflect $R \gg R_0 > R_n$, the dominant term on the far left side is the term proportional to $R^2 = A/\pi$, where $A$ is the TEM area. These considerations yield the following estimate of $\sigma_0$:

$$\frac{\sigma_0}{\mu} = \frac{A_2 - A_1}{4\pi\Delta t}, \quad (9)$$

where $\Delta t$ = 1 s is the time interval between two acquisitions; $A_1$ is the TEM area in the first image after TEM opening (taken on average at a time $\Delta t/2$), and $A_2$ is the TEM area in the second image.

| Condition | $\sigma_0$ (μN/m) | $A_{max}$ (μm$^2$) | $N$ (average) | $(N \cdot A_{max})^{-1}$ (μm$^{-2}$) |
|---|---|---|---|---|
| Control | 25 ± 10 | 8.1 ± 0.5 | 0.90 ± 0.09 | 0.137 ± 0.022 |
| siCAV1 | 50 ± 7 | 23 ± 4 | 1.92 ± 0.15 | 0.023 ± 0.006 |
| siPTRF | 29 ± 7 | 9.3 ± 0.7 | 1.34 ± 0.11 | 0.080 ± 0.012 |

**Table 2.** Estimate of the variation of mechanical cell parameters between different experimental conditions. The value of the effective membrane tension $\sigma_0$ for the control case is obtained from earlier estimates (*65*). The increase in $\sigma_0$ for siCAV1 and siPTRF cell membranes is deduced from our experimental data using Eq. 9. The TEM maximum area, $A_{max}$, is the median not the average value because the median is a more robust estimator in the presence of a few extremely large values. As discussed in the text, the variations in the bending rigidity are roughly proportional to variations in $(N \cdot A_{max})^{-1}$, where $N$ is the average number of TEMs opening simultaneously and $A_{max}$ is the TEM maximum area.

657
658 **Statistical analysis**
659 Statistical tests were performed using the R Software v4.2.1(R Foundation for Statistical
660 Computing, Vienna, Austria. https://www.R-project.org/), along with packages lme4 (1.1-30)(*72*),
661 lmerTest (v3.1-3)(*73*), emmeans (v1.8.0) (https://CRAN.R-project.org/package=emmeans), except
662 for the F-actin mesh size where the Prism Software was used. All experiments were repeated at
663 least three times to ensure reproducibility and corresponding variability was accounted for in
664 statistical analyses using mixed-effect regressions, with a random intercept estimated for every
665 technical replicate. In particular, Binomial outcomes (e.g. presence/absence) were analysed using
666 mixed-effect logistic regression. Continuous measurements (e.g. TEM area) were investigated with
667 a Gamma log-link function in a mixed-effect framework. Contrasts between multiple pairs of
668 categorical predictors were calculated through estimated marginal means with Tukey's correction.
669 P-values were calculated as indicated in the respective figure legends. P-values were considered
670 statistically significant at $P \leq 0.05$. Significance levels are indicated as follows: ns: not significant
671 if $P > 0.05$; * : $P \leq 0.05$; **: $P \leq 0.01$; ***: $P \leq 0.001$; ****: $\leq 0.0001$.
672

673
674
675 **H2: Supplementary Materials**
676
677 Fig. S1. $CAV1^{+/+}$ mice susceptibility to EDIN-B in Staphylococcal septicaemia
678 Fig. S2. Controls of siRNAs and RhoA ADP-ribosylation efficacies.
679 Fig. S3. Caveolin-1 and cavin-1/PTRF depletion increases TEM formation in both ExoC3- and
680 EDIN-treated cells.
681 Fig. S4. Depletion of the caveolar accessory component EHD2 increases the TEM tunnel
682 formation
683 Fig. S5. Caveolin-1 controls the TEM opening speed and maximum size.
684
685 **References and Notes**
686
687 1. W. C. Aird, Phenotypic heterogeneity of the endothelium: II. Representative vascular beds.
688 *Circ Res* **100**, 174–190 (2007).
689 2. W. C. Aird, Phenotypic heterogeneity of the endothelium: I. Structure, function, and
690 mechanisms. *Circ Res* **100**, 158–173 (2007).
691 3. Y. A. Komarova, K. Kruse, D. Mehta, A. B. Malik, Protein Interactions at Endothelial
692 Junctions and Signaling Mechanisms Regulating Endothelial Permeability. *Circ Res* **120**,
693 179–206 (2017).
694 4. L. Guo, H. Zhang, Y. Hou, T. Wei, J. Liu, Plasmalemma vesicle-associated protein: A crucial
695 component of vascular homeostasis. *Exp Ther Med* **12**, 1639–1644 (2016).
696 5. E. Lemichez, D. Gonzalez-Rodriguez, P. Bassereau, F. Brochard-Wyart, Transcellular tunnel
697 dynamics: Control of cellular dewetting by actomyosin contractility and I-BAR proteins. *Biol*
698 *Cell* **105**, 109–117 (2013).
699 6. S. T. Braakman, A. T. Read, D. W. Chan, C. R. Ethier, D. R. Overby, Colocalization of
700 outflow segmentation and pores along the inner wall of Schlemm's canal. *Exp Eye Res* **130**,
701 87–96 (2015).
702 7. S. Barzilai, S. K. Yadav, S. Morrell, F. Roncato, E. Klein, L. Stoler-Barak, O. Golani, S. W.
703 Feigelson, A. Zemel, S. Nourshargh, R. Alon, Leukocytes Breach Endothelial Barriers by
704 Insertion of Nuclear Lobes and Disassembly of Endothelial Actin Filaments. *Cell Rep* **18**,
705 685–699 (2017).

8. L. Boyer, A. Doye, M. Rolando, G. Flatau, P. Munro, P. Gounon, R. Clement, C. Pulcini, M. R. Popoff, A. Mettouchi, L. Landraud, O. Dussurget, E. Lemichez, Induction of transient macroapertures in endothelial cells through RhoA inhibition by Staphylococcus aureus factors. *J Cell Biol* **173**, 809–819 (2006).
9. D. Gonzalez-Rodriguez, C. Morel, E. Lemichez, Dewetting: From Physics to the Biology of Intoxicated Cells. *Adv Exp Med Biol* **1267**, 101–115 (2020).
10. M. P. Maddugoda, C. Stefani, D. Gonzalez-Rodriguez, J. Saarikangas, S. Torrino, S. Janel, P. Munro, A. Doye, F. Prodon, M. Aurrand-Lions, P. L. Goossens, F. Lafont, P. Bassereau, P. Lappalainen, F. Brochard, E. Lemichez, cAMP signaling by anthrax edema toxin induces transendothelial cell tunnels, which are resealed by MIM via Arp2/3-driven actin polymerization. *Cell Host Microbe* **10**, 464–474 (2011).
11. M. Sugai, K. Hashimoto, A. Kikuchi, S. Inoue, H. Okumura, K. Matsumoto, Y. Goto, H. Ohgai, K. Moriishi, B. Syuto, Epidermal cell differentiation inhibitor ADP-ribosylates small GTP-binding proteins and induces hyperplasia of epidermis. *J Biol Chem* **267**, 2600–2604 (1992).
12. P. Chardin, P. Boquet, P. Madaule, M. R. Popoff, E. J. Rubin, D. M. Gill, The mammalian G protein rhoC is ADP-ribosylated by Clostridium botulinum exoenzyme C3 and affects actin microfilaments in Vero cells. *Embo J* **8**, 1087–1092 (1989).
13. H. F. Paterson, A. J. Self, M. D. Garrett, I. Just, K. Aktories, A. Hall, Microinjection of recombinant p21rho induces rapid changes in cell morphology. *J Cell Biol* **111**, 1001–1007 (1990).
14. W. P. Ng, K. D. Webster, C. Stefani, E. M. Schmid, E. Lemichez, P. Bassereau, D. A. Fletcher, Force-induced transcellular tunnel formation in endothelial cells. *Mol Biol Cell* **doi: 10.1091/mbc.E17-01-0080**, 2650–2660 (2017).
15. M. C. Tsai, L. Fleuriot, S. Janel, D. Gonzalez-Rodriguez, C. Morel, A. Mettouchi, D. Debayle, S. Dallongeville, J. C. Olivo-Marin, B. Antonny, F. Lafont, E. Lemichez, H. Barelli, DHA-containing phospholipids control membrane fusion and transcellular tunnel dynamics. *J Cell Sci* **135**, doi: 10.1242/jcs.259119 (2022).
16. M. Rolando, P. Munro, C. Stefani, P. Auberger, G. Flatau, E. Lemichez, Injection of Staphylococcus aureus EDIN by the Bacillus anthracis protective antigen machinery induces vascular permeability. *Infect Immun* **77**, 3596–3601 (2009).
17. P. Munro, M. Benchetrit, M. A. Nahori, C. Stefani, R. Clement, J. F. Michiels, L. Landraud, O. Dussurget, E. Lemichez, Staphylococcus aureus EDIN toxin promotes formation of infection foci in a mouse model of bacteremia. *Infect Immun* **78**, 3404–3411 (2010).
18. J. Courjon, P. Munro, Y. Benito, O. Visvikis, C. Bouchiat, L. Boyer, A. Doye, H. Lepidi, E. Ghigo, J. P. Lavigne, F. Vandenesch, E. Lemichez, EDIN-B Promotes the Translocation of Staphylococcus aureus to the Bloodstream in the Course of Pneumonia. *Toxins (Basel)* **7**, 4131–4142 (2015).
19. D. Gonzalez-Rodriguez, K. Guevorkian, S. Douezan, F. Brochard-Wyart, Soft matter models of developing tissues and tumors. *Science* **338**, 910–917 (2012).
20. A. Charles-Orszag, E. Lemichez, G. Tran Van Nhieu, G. Duménil, Microbial pathogenesis meets biomechanics. *Curr Opin Cell Biol* **38**, 31–37 (2016).
21. D. Gonzalez-Rodriguez, M. P. Maddugoda, C. Stefani, S. Janel, F. Lafont, D. Cuvelier, E. Lemichez, F. Brochard-Wyart, Cellular dewetting: opening of macroapertures in endothelial cells. *Phys Rev Lett* **108**, 218105 (2012).
22. B. Sinha, D. Köster, R. Ruez, P. Gonnord, M. Bastiani, D. Abankwa, R. V. Stan, G. Butler-Browne, B. Vedie, L. Johannes, N. Morone, R. G. Parton, G. Raposo, P. Sens, C. Lamaze, P. Nassoy, Cells respond to mechanical stress by rapid disassembly of caveolae. *Cell* **144**, 402–413 (2011).

23. R. G. Parton, M. Hanzal-Bayer, J. F. Hancock, Biogenesis of caveolae: a structural model for caveolin-induced domain formation. *J Cell Sci* **119**, 787–796 (2006).
24. J. C. Porta, B. Han, A. Gulsevin, J. M. Chung, Y. Peskova, S. Connolly, H. S. Mchaourab, J. Meiler, E. Karakas, A. K. Kenworthy, M. D. Ohi, Molecular architecture of the human caveolin-1 complex. *Sci Adv* **8**, eabn7232 (2022).
25. A. Ludwig, G. Howard, C. Mendoza-Topaz, T. Deerinck, M. Mackey, S. Sandin, M. H. Ellisman, B. J. Nichols, Molecular composition and ultrastructure of the caveolar coat complex. *PLoS Biol* **11**, e1001640 (2013).
26. N. Ariotti, J. Rae, N. Leneva, C. Ferguson, D. Loo, S. Okano, M. M. Hill, P. Walser, B. M. Collins, R. G. Parton, Molecular Characterization of Caveolin-induced Membrane Curvature. *J Biol Chem* **290**, 24875–24890 (2015).
27. A. Ludwig, B. J. Nichols, S. Sandin, Architecture of the caveolar coat complex. *J Cell Sci* **129**, 3077–3083 (2016).
28. L. Yang, S. Scarlata, Super-resolution Visualization of Caveola Deformation in Response to Osmotic Stress. *J Biol Chem* **292**, 3779–3788 (2017).
29. C. Lamaze, N. Tardif, M. Dewulf, S. Vassilopoulos, C. M. Blouin, The caveolae dress code: structure and signaling. *Curr Opin Cell Biol* **47**, 117–125 (2017).
30. O. Daumke, R. Lundmark, Y. Vallis, S. Martens, P. J. Butler, H. T. McMahon, Architectural and mechanistic insights into an EHD ATPase involved in membrane remodelling. *Nature* **449**, 923–927 (2007).
31. I. Yeow, G. Howard, J. Chadwick, C. Mendoza-Topaz, C. G. Hansen, B. J. Nichols, E. Shvets, EHD Proteins Cooperate to Generate Caveolar Clusters and to Maintain Caveolae during Repeated Mechanical Stress. *Curr Biol* **27**, 2951–2962.e5 (2017).
32. T. Nishimura, S. Suetsugu, Super-resolution analysis of PACSIN2 and EHD2 at caveolae. *PLoS One* **17**, e0271003 (2022).
33. J. Yu, S. Bergaya, T. Murata, I. F. Alp, M. P. Bauer, M. I. Lin, M. Drab, T. V. Kurzchalia, R. V. Stan, W. C. Sessa, Direct evidence for the role of caveolin-1 and caveolae in mechanotransduction and remodeling of blood vessels. *J Clin Invest* **116**, 1284–1291 (2006).
34. M. A. Del Pozo, F. N. Lolo, A. Echarri, Caveolae: Mechanosensing and mechanotransduction devices linking membrane trafficking to mechanoadaptation. *Curr Opin Cell Biol* **68**, 113–123 (2021).
35. M. R. Siddiqui, Y. A. Komarova, S. M. Vogel, X. Gao, M. G. Bonini, J. Rajasingh, Y. Y. Zhao, V. Brovkovych, A. B. Malik, Caveolin-1-eNOS signaling promotes p190RhoGAP-A nitration and endothelial permeability. *J Cell Biol* **193**, 841–850 (2011).
36. B. Razani, J. A. Engelman, X. B. Wang, W. Schubert, X. L. Zhang, C. B. Marks, F. Macaluso, R. G. Russell, M. Li, R. G. Pestell, D. Di Vizio, H. Hou, B. Kneitz, G. Lagaud, G. J. Christ, W. Edelmann, M. P. Lisanti, Caveolin-1 null mice are viable but show evidence of hyperproliferative and vascular abnormalities. *J Biol Chem* **276**, 38121–38138 (2001).
37. K. Miyawaki-Shimizu, D. Predescu, J. Shimizu, M. Broman, S. Predescu, A. B. Malik, siRNA-induced caveolin-1 knockdown in mice increases lung vascular permeability via the junctional pathway. *Am J Physiol Lung Cell Mol Physiol* **290**, L405–13 (2006).
38. F. S. Machado, N. E. Rodriguez, D. Adesse, L. R. Garzoni, L. Esper, M. P. Lisanti, R. D. Burk, C. Albanese, K. Van Doorslaer, L. M. Weiss, F. Nagajyothi, J. D. Nosanchuk, M. E. Wilson, H. B. Tanowitz, Recent developments in the interactions between caveolin and pathogens. *Adv Exp Med Biol* **729**, 65–82 (2012).
39. A. N. Spaan, A. L. Neehus, E. Laplantine, F. Staels, M. Ogishi, Y. Seeleuthner, F. Rapaport, K. A. Lacey, E. Van Nieuwenhove, M. Chrabieh, D. Hum, M. Migaud, A. Izmiryan, L. Lorenzo, T. Kochetkov, D. A. C. Heesterbeek, B. W. Bardoel, A. L. DuMont, K. Dobbs, S. Chardonnet, S. Heissel, T. Baslan, P. Zhang, R. Yang, D. Bogunovic, H. F. Wunderink, P. A. Haas, H. Molina, G. Van Buggenhout, S. Lyonnet, L. D. Notarangelo, M. R. J. Seppänen, R.

Weil, G. Seminario, H. Gomez-Tello, C. Wouters, M. Mesdaghi, M. Shahrooei, X. Bossuyt, E. Sag, R. Topaloglu, S. Ozen, H. L. Leavis, M. M. J. van Eijk, L. Bezrodnik, L. Blancas Galicia, A. Hovnanian, A. Nassif, B. Bader-Meunier, B. Neven, I. Meyts, R. Schrijvers, A. Puel, J. Bustamante, I. Aksentijevich, D. L. Kastner, V. J. Torres, S. Humblet-Baron, A. Liston, L. Abel, B. Boisson, J. L. Casanova, Human OTULIN haploinsufficiency impairs cell-intrinsic immunity to staphylococcal α-toxin. *Science* **376**, eabm6380 (2022).

40. F. A. Medina, C. J. de Almeida, E. Dew, J. Li, G. Bonuccelli, T. M. Williams, A. W. Cohen, R. G. Pestell, P. G. Frank, H. B. Tanowitz, M. P. Lisanti, Caveolin-1-deficient mice show defects in innate immunity and inflammatory immune response during Salmonella enterica serovar Typhimurium infection. *Infect Immun* **74**, 6665–6674 (2006).
41. M. M. Hill, M. Bastiani, R. Luetterforst, M. Kirkham, A. Kirkham, S. J. Nixon, P. Walser, D. Abankwa, V. M. Oorschot, S. Martin, J. F. Hancock, R. G. Parton, PTRF-Cavin, a conserved cytoplasmic protein required for caveola formation and function. *Cell* **132**, 113–124 (2008).
42. E. Zlotek-Zlotkiewicz, S. Monnier, G. Cappello, M. Le Berre, M. Piel, Optical volume and mass measurements show that mammalian cells swell during mitosis. *J Cell Biol* **211**, 765–774 (2015).
43. S. Torrino, W. W. Shen, C. M. Blouin, S. K. Mani, C. Viaris de Lesegno, P. Bost, A. Grassart, D. Köster, C. A. Valades-Cruz, V. Chambon, L. Johannes, P. Pierobon, V. Soumelis, C. Coirault, S. Vassilopoulos, C. Lamaze, EHD2 is a mechanotransducer connecting caveolae dynamics with gene transcription. *J Cell Biol* **217**, 4092–4105 (2018).
44. W. Helfrich, Elastic properties of lipid bilayers: theory and possible experiments. *Z Naturforsch C* **28**, 693–703 (1973).
45. D. Raucher, M. P. Sheetz, Cell spreading and lamellipodial extension rate is regulated by membrane tension. *J Cell Biol* **148**, 127–136 (2000).
46. L. Bo, R. E. Waugh, Determination of bilayer membrane bending stiffness by tether formation from giant, thin-walled vesicles. *Biophys J* **55**, 509–517 (1989).
47. D. Lingwood, J. Ries, P. Schwille, K. Simons, Plasma membranes are poised for activation of raft phase coalescence at physiological temperature. *Proc Natl Acad Sci U S A* **105**, 10005–10010 (2008).
48. I. Derényi, F. Jülicher, J. Prost, Formation and interaction of membrane tubes. *Phys Rev Lett* **88**, 238101 (2002).
49. B. P. Manneville J.-B., Levy D., Prost J., Activity of transmembrane proteins induces magnification of shape fluctuations of lipid membranes. *Phys. Rev. Lett.* **82**, 4356–4359 (1999).
50. P. J. Girard P., Bassereau P., Passive or active fluctuations in membranes containing proteins. *Phys. Rev. Lett.* **94**, 088102 (2005).
51. H. J. Fowler P. W., Duncan A., Chavent M., Koldso H., Sansom M. S. P., Membrane stiffness is modified by integral membrane proteins. *Soft Matter* **12**, 7792–7803 (2016).
52. N. Roitenberg, M. Bejerano-Sagie, H. Boocholez, L. Moll, F. C. Marques, L. Golodetzki, Y. Nevo, T. Elami, E. Cohen, Modulation of caveolae by insulin/IGF-1 signaling regulates aging of Caenorhabditis elegans. *EMBO Rep* **19**, (2018).
53. R. G. Parton, M. M. Kozlov, N. Ariotti, Caveolae and lipid sorting: Shaping the cellular response to stress. *J Cell Biol* **219**, (2020).
54. W. Rawicz, B. A. Smith, T. J. McIntosh, S. A. Simon, E. Evans, Elasticity, strength, and water permeability of bilayers that contain raft microdomain-forming lipids. *Biophys J* **94**, 4725–4736 (2008).
55. K. Xie, Y. Yang, H. Jiang, Controlling Cellular Volume via Mechanical and Physical Properties of Substrate. *Biophys J* **114**, 675–687 (2018).

56. I. Carton, D. Trouet, D. Hermans, H. Barth, K. Aktories, G. Droogmans, N. K. Jorgensen, E. K. Hoffmann, B. Nilius, J. Eggermont, RhoA exerts a permissive effect on volume-regulated anion channels in vascular endothelial cells. *Am J Physiol Cell Physiol* **283**, C115–25 (2002).
57. P. Jansa, C. Burek, E. E. Sander, I. Grummt, The transcript release factor PTRF augments ribosomal gene transcription by facilitating reinitiation of RNA polymerase I. *Nucleic Acids Res* **29**, 423–429 (2001).
58. P. Jansa, I. Grummt, Mechanism of transcription termination: PTRF interacts with the largest subunit of RNA polymerase I and dissociates paused transcription complexes from yeast and mouse. *Mol Gen Genet* **262**, 508–514 (1999).
59. L. Liu, P. F. Pilch, PTRF/Cavin-1 promotes efficient ribosomal RNA transcription in response to metabolic challenges. *Elife* **5**, (2016).
60. Y. Shi, S. H. Tan, S. Ng, J. Zhou, N. D. Yang, G. B. Koo, K. A. McMahon, R. G. Parton, M. M. Hill, M. A. Del Pozo, Y. S. Kim, H. M. Shen, Critical role of CAV1/caveolin-1 in cell stress responses in human breast cancer cells via modulation of lysosomal function and autophagy. *Autophagy* **11**, 769–784 (2015).
61. Y. Gillet, A. Tristan, J. P. Rasigade, M. Saadatian-Elahi, C. Bouchiat, M. Bes, O. Dumitrescu, M. Leloire, C. Dupieux, F. Laurent, G. Lina, J. Etienne, P. Vanhems, L. Argaud, F. Vandenesch, P. S. G. PVL, Prognostic factors of severe community-acquired staphylococcal pneumonia in France. *Eur Respir J* **58**, (2021).
62. M. Perret, C. Badiou, G. Lina, S. Burbaud, Y. Benito, M. Bes, V. Cottin, F. Couzon, C. Juruj, O. Dauwalder, N. Goutagny, B. A. Diep, F. Vandenesch, T. Henry, Cross-talk between Staphylococcus aureus leukocidins-intoxicated macrophages and lung epithelial cells triggers chemokine secretion in an inflammasome-dependent manner. *Cell Microbiol* **14**, 1019–1036 (2012).
63. A. Tristan, M. Bes, H. Meugnier, G. Lina, B. Bozdogan, P. Courvalin, M. E. Reverdy, M. C. Enright, F. Vandenesch, J. Etienne, Global distribution of Panton-Valentine leukocidin--positive methicillin-resistant Staphylococcus aureus, 2006. *Emerg Infect Dis* **13**, 594–600 (2007).
64. A. Doye, A. Mettouchi, G. Bossis, R. Clement, C. Buisson-Touati, G. Flatau, L. Gagnoux, M. Piechaczyk, P. Boquet, E. Lemichez, CNF1 exploits the ubiquitin-proteasome machinery to restrict Rho GTPase activation for bacterial host cell invasion. *Cell* **111**, 553–564 (2002).
65. C. Stefani, D. Gonzalez-Rodriguez, Y. Senju, A. Doye, N. Efimova, S. Janel, J. Lipuma, M. C. Tsai, D. Hamaoui, M. P. Maddugoda, O. Cochet-Escartin, C. Prévost, F. Lafont, T. Svitkina, P. Lappalainen, P. Bassereau, E. Lemichez, Ezrin enhances line tension along transcellular tunnel edges via NMIIa driven actomyosin cable formation. *Nat Commun* **8**, 15839 (2017).
66. D. Cuvelier, I. Derényi, P. Bassereau, P. Nassoy, Coalescence of membrane tethers: experiments, theory, and applications. *Biophys J* **88**, 2714–2726 (2005).
67. B. Sorre, A. Callan-Jones, J. B. Manneville, P. Nassoy, J. F. Joanny, J. Prost, B. Goud, P. Bassereau, Curvature-driven lipid sorting needs proximity to a demixing point and is aided by proteins. *Proc Natl Acad Sci U S A* **106**, 5622–5626 (2009).
68. Evans, Rawicz, Entropy-driven tension and bending elasticity in condensed-fluid membranes. *Phys Rev Lett* **64**, 2094–2097 (1990).
69. K. Guevorkian, D. Gonzalez-Rodriguez, C. Carlier, S. Dufour, F. Brochard-Wyart, Mechanosensitive shivering of model tissues under controlled aspiration. *Proc Natl Acad Sci U S A* **108**, 13387–13392 (2011).
70. A. Al Jord, G. Letort, S. Chanet, F. C. Tsai, C. Antoniewski, A. Eichmuller, C. Da Silva, J. R. Huynh, N. S. Gov, R. Voituriez, M. E. Terret, M. H. Verlhac, Cytoplasmic forces functionally reorganize nuclear condensates in oocytes. *BioRxiv* 10.1101/2021.03.15.434387

71. S. van der Walt, J. L. Schönberger, J. Nunez-Iglesias, F. Boulogne, J. D. Warner, N. Yager, E. Gouillart, T. Yu, C. scikit-image, scikit-image: image processing in Python. *PeerJ* **2**, e453 (2014).
72. D. Bates, M. Mächler, B. Bolker, S. Walker, Fitting Linear Mixed-Effects Models Using lme4. *Journal of Statistical Software* **67**, 1 - 48 (2015).
73. A. Kuznetsova, P. B. Brockhoff, R. H. B. Christensen, lmerTest Package: Tests in Linear Mixed Effects Models. *Journal of Statistical Software* **82**, 1 - 26 (2017).

## Acknowledgements

**General**: C. Morel and E. Lemerle were supported by PhD fellowships from the University Paris Cité Doctoral School BioSPC and Sorbonne University Doctoral School complexité du vivant, respectively. We thank Amel Mettouchi, Arnaud Echard, Virginia Ribeiro de Andrade (Institut Pasteur, Paris, France) and Michael Henderson (Institut Pasteur/Institut Curie, Paris France) for technical advice, sharing reagents and for discussions. We thank Pierre Nassoy (LP2N, Bordeaux, France), Francoise Brochard Wyart (Institut Curie, Paris, France), and Anne Blangy (CRBM, CNRS, Montpellier, France) for insightful discussions. We thank Darius Koster for sharing results and for fruitful discussions on tether pulling experiments of plasma membrane spheres. We thank Gaëlle Letort (Department of Developmental and Stem Cell Biology, Institut Pasteur, CNRS UMR 3738) for helpful advice on image analysis. We also thank the UTechS PBI, which is part of the France–BioImaging infrastructure network (FBI) supported by the French National Research Agency (ANR-10-INBS-04; Investments for the Future) and acknowledges support from Institut Pasteur, ANR/FBI, the Région Ile-de-France (program DIM1HEALTH), and the French Government Investissement d'Avenir Programme-Laboratoire d'Excellence 'Integrative Biology of Emerging Infectious Diseases' (ANR-10-LABX-62-IBEID) for the use of the Zeiss ELYRA7 microscope.

**Funding:** Include all funding sources, including grant numbers and funding agencies.

**Author contributions:** Animal experiments were performed by M-A.N. and C.M.; cell biology experiments were performed by C.M.; biochemistry experiments were performed by C.S., M.M. and C.M.; the physical model was established by D.G-R. All statistical analyses were performed by C.M. and T.O.; cell volume measurements were performed by C.M. and N.S. together with M.P.; transmission electron microscopy was performed by C.M. and E.L. together with S.V. Super-resolution imaging was performed by C.M., A.S., and C.Le.; bending rigidity measurements were performed by C.M. and F.C-T. together with P.B.; video and image analyses were performed by C.M., C.Le. and M.A.; E. Lemichez and C.Le. designed the experiments and supervised the project. E. Lemichez, C.Le., D. G-R, C.M., C. La and P.B. wrote the manuscript. All authors reviewed the manuscript.

**Competing interests:** The authors declare no competing interest.

**Data and materials availability:** All data needed to evaluate the conclusions in the paper are presented in the paper and/or the Supplementary Materials.

## FIGURES AND TABLES

**Fig. 1. Susceptibility of CAV1-deficient mice to EDIN-B exoenzyme in *S. aureus* bacteremia.**

(**A-C**) Kaplan–Meier survival curves over 7 days for groups of $CAV1^{-/-}$ mice and $CAV1^{+/+}$ littermates infected intravenously at Day 0 with different doses, expressed as colony-forming units per mouse (CFU/m), of LUG1799 wild-type *S. aureus*, which is positive for *edinB* (WT *edinB*), and the isogenic strain LUG1840 I, in which the *edinB*-encoding gene (Δ*edinB*) is deleted. (**A**) Comparative analysis of $CAV1^{-/-}$ and $CAV1^{+/+}$ mouse susceptibility to *S. aureus* bacteraemia. Groups of $CAV1^{-/-}$ and $CAV1^{+/+}$ mice were challenged via intravenous injection of $5\times10^6$ CFU/mouse ($n$=10 $CAV1^{+/+}$ mice vs. $n$=9 $CAV1^{-/-}$ mice), $5\times10^7$ CFU/mouse ($n$=7 $CAV1^{+/+}$ mice vs. $n$=9 $CAV1^{-/-}$ mice) or $5\times10^8$ CFU/mouse ($n$=7 $CAV1^{+/+}$ mice vs. $n$=8 $CAV1^{-/-}$ mice). After administering a dose of $5\times10^7$ CFU/mouse, we recorded a significant increase in $CAV1^{-/-}$ susceptibility to infection compared with that of the $CAV1^{+/+}$ littermates. Log-rank test (Mantel–Cox), $P < 0.0011$ at $5\times10^7$ CFU/mouse (1 experiment). (**B**) Lethal dose 50 ($LD_{50}$) of WT *edinB* or Δ*edinB* strains administered to mice. Mice were injected with $2.5\times10^7$ CFU/mouse ($n$=12 mice infected with either WT *edinB* or Δ *edinB* strains, 2 experiments). There were no significant difference in the survival kinetics between WT *edinB*- and Δ*edinB*-infected animals, as determined by log-rank test (Mantel–Cox). (**C**) Comparative analysis of the susceptibility of $CAV1^{-/-}$ mice to bloodstream infection triggered by either the WT or Δ*edinB* strains. Mice were injected with $2.5\times10^7$ CFU/mouse ($n$=17 and 18 mice infected with WT and Δ*edinB* strains, from 2 experiments). Log-rank test (Mantel–Cox) showed a significantly higher susceptibility of $CAV1^{-/-}$ mice to WT *edinB* than to Δ*edinB* ($P$=0.0123).

**Fig. 2. High number of TEMs in caveolin-1- or cavin-1/PTRF-depleted cells.**

(**A**) Confocal spinning disk images showing the actin cytoskeleton of HUVECs treated with an siRNA control (siCTRL) and siRNA against caveolin-1 (siCAV1) and cavin-1 (siPTRF) and left untreated (Control) or treated for 24 h with C3 exoenzyme (ExoC3). Cells were stained with phalloidin-TRITC. Arrowheads show the presence of stress fibres in the absence of ExoC3 treatment. Stars show examples of TEM tunnels surrounded by thick actin cables. Scale bar, 20 µm. (**B**) Histograms show the percentages of ExoC3-treated cells displaying at least one TEM ($n$=1,400 cells per condition in 8 independent experiments). Graph shows technical replicates pooled together. Error bars show normal asymptotic 95% confidence intervals (CI). Data analysis with mixed-effect logistic regression model (random intercept capturing technical variability) with correction for multiple comparisons using a Tukey's HSD test. ****$P$<0.0001, for both siCTRL vs siCAV1 and siCTRL vs siPTRF conditions. No difference was recorded between siCAV1 and siPTRF conditions.

**Fig. 3. Regulation of HUVEC area and volume by cavin-1/PTRF, caveolin-1 and RhoA.**

**(A**) Confocal spinning disk images of HUVECs stained with phalloidin-FITC and selected perimeters (yellow line) in the absence (- ExoC3) or presence of ExoC3 (+ ExoC3). Scale bar, 20 µm. (**B**) Schematic representation of the device used to define the volume of a cell by measuring the intensity of fluorescence exclusion. Briefly, from the top to the bottom, i) side view of the chamber in which a cell adheres to a coverslip. The PDMS pillar sustains the ceiling (grey), and the maximal height of the chamber $h_{max}$ (background) is known. The siCTRL-, siCAV1- or siPTRF-transfected HUVECs were seeded in the chamber and remained either untreated or treated with ExoC3. High molecular weight dextran-FITC (green) was added to the chamber being and was excluded from cells (values $h_{x,y}$). ii) Raw epifluorescence image showing a typical field of HUVECs

and iii) the graph of fluorescence intensities (in greyscale) which show the function of distance along the dotted line. Parameters $I_{max}$ and $I_{min}$ yield values of maximum and minimum fluorescence intensities. Values for cell volume ($V_{cell}$) were obtained by integrating the fluorescence intensities $h_{max} - h_{x,y}$ over the cell area. (**C**) Boxplots show the distribution of values of areas with TEMs as estimated from measures of their perimeters, which is shown in (a). Measurements were performed with HUVECs transfected with siCTRL, siCAV1 or siPTRF and then treated with ExoC3 (+ ExoC3) or untreated (- ExoC3). Measurements were performed with $n$>698 untreated cells and $n$>595 treated cells, 5 independent experiments. (**D**) Boxplots show the distribution of cell volumes, as described in (c). Measurements were performed on HUVECs transfected with siCTRL, siCAV1 or siPTRF and then treated with ExoC3 (+ ExoC3) or untreated (- ExoC3). Data are from $n$=216 and $n$=308 cells after siCTRL ± ExoC3 treatment, $n$=197 and $n$=266 cells after siCAV1 ± ExoC3 treatment and $n$=152 and $n$=157 cells after siPTRF ± ExoC3 treatment; 3 independent experiments. (**B-D**). Graph shows technical replicates pooled together. The data were analysed with a mixed-effect generalized linear model with Gamma log-link function, random intercept accounting for technical variability and Tukey's correction for pairwise comparisons between control and each siRNA treatment, ****$P$<0.0001, **$P$<0.01, *$P$<0.05 and ns, not significant.

**Fig. 4. Inhibition of RhoA decreases caveolae density on the plasma membrane and loosens the F-actin meshwork**.

(**A-B**) Transmission electron micrographs show unroofed HUVECs that were either untreated (- ExoC3) or treated with ExoC3 (+ ExoC3); caveolae on the ventral side of the plasma membrane are evident (**A**) and anti-GFP immunogold-labelled GFP-caveolin-1 is shown (**B**). Right panels show membrane areas at high magnification, revealing i) caveolae (plain yellow arrowhead), ii) clathrin-coated pits and patches (plain white arrowhead), iii) actin filaments (empty white arrowhead) and TEM tunnels in treated cells (white star). (**B**) Immunogold labelled GFP-CAV1 as shown in (**A**). Gold beads are represented by yellow circles. (**A-B**) Scale bars: control, 1 µm; high magnification, 200 nm; ExoC3, 5 µm; high magnification, 200 nm. (**C**) Boxplot shows the density of caveolae per µm$^2$ of the plasma membrane in control versus ExoC3-treated HUVEC. Quantification was performed on transmission electron micrographs, see examples in (A). Graph shows technical replicates pooled together. Data were analysed with a mixed-effects linear model with random intercept and Tukey's correction for pairwise comparison. *$P$= 0.027 ($n$=16 cells from 3 technical replicates). (**D**) 2D STORM images show the disruption of actin bundles and the highly dense meshwork consisting of intertwined actin filaments with F-actin in a loose meshwork. HUVECs were transfected with siCTRL, siCAV1 or siPTRF and either left untreated or treated with ExoC3 before F-actin staining with phalloidin. Scale bar, 10 µm. High magnification images are shown in the right panels. Scale bar, 1 µm. **(E)** Boxplot shows the average mesh size per cell (µm²) of the F-actin network. Quantification was performed with 2D STORM images of siCTRL-, siCAV1- and siPTRF-treated cells, denoted (+), and ExoC3-treated cells (-). $P$ values were calculated with a nested t test on 8 to 9 cells per group; 3 independent replicates. **$P$<0.01, *$P$<0.05

**Fig. 5. Caveolin-1 controls the TEM opening speed and maximum size**.

**(A)** Images show examples of projections of all tunnels upon TEM initial opening (lower panel) in HUVECs transfected with Lifeact-GFP expression plasmid and siCTRL, siCAV1 or siPTRF captured during 1 h of live imaging. Lifeact-GFP HUVECs transfected with different siRNAs were treated with ExoC3 and recorded by live imaging for 1 h. All initial TEM opening was based on the first frame in which TEM tunnels formed using ICY. The lower panel shows the projection of cumulative areas of initial TEM opening identified during 1 h of live imaging. Scale bars, 20 µm. **(B)** Boxplot shows the distribution of TEMs, the maximal and median area values in HUVECs cotransfected with Lifeact-GFP expressing plasmid and siCTRL, siCAV1, or siPTRF prior ExoC3

treatment. Maximal areas were determined on the basis of each kinetic parameter of TEM dynamics, as shown in (C). The data represent *n*>105 TEMs in 7 cells of each treatment group; >3 independent experiments. Graph shows technical replicates pooled together. Statistical data analysis using a mixed-effect generalized linear model with Gamma log-link function, random intercept, and Tukey's correction for multiple comparisons. ****P<0.0001, **P<0.01 and ns, non-significant. **(C)** The graph shows variations in TEM areas as a function of time expressed in minutes. HUVECs transfected with siCTRL, siCAV1 or siPTRF were treated with ExoC3 for 24 h. The calculated values of $t_{max}$ that corresponded to the time of opening to the time when the maximal areas were observed and the values of tc corresponded to the time frame of a complete cycle of opening and closing are indicated on the graph for each condition. The data are from *n*>105 TEMs of 7 cells per treatment; >3 independent experiments. **(D)** The graph shows variations in mean values, expressed in seconds, in the TEM areas of cells treated with ExoC3. The curves were plotted with data obtained from time-lapse video recorded at 1 frame/second for 30 min. Lifeact-GFP expressing cells transfected with siCTRL, siCAV1, and siPTRF. The data correspond to *n*> 22 TEMs per condition from 4 independent experiments.

**Fig. 6. Caveolin-1 controls membrane bending and rigidity.**

(**A**) Confocal spinning disk image of a HUVEC displaying a calcein-AM-positive attached plasma membrane sphere (PMS) (arrowhead). Scale bar, 10 µm. (**B**) Schematic representation of the device used for measuring membrane mechanical parameters. It shows micropipette aspiration (grey) of a PMS (blue) and a tube pulled from the PMS through a bead bound to the PMS and trapped with an optical tweezer (purple). Increasing the aspiration pressure in the pipette allowed a progressive increase in the PMS membrane tension. (**C**) Confocal images show examples of calcein-AM-positive PMSs prepared from siCTRL-, siCAV1- or siPTRF-transfected cells during micropipette aspiration. Scale bars, 2 µm. (**D**) the Force required to pull membrane tubes rescaled to $((f-f_0)^2/8\pi^2)$ (in $pN^2$), which is a function of the membrane tension (mN/m) for different siCTRL, siCAV1 and siPTRF treatments. The force $f_0$ was measured for each tube as the force when the membrane tension vanishes. The bending rigidity $\kappa$ (in $k_BT$) was determined via the slope of the linear regression. The data were calculated from *n*=5 to *n*=10 tubes per condition (>4 independent experiments). Linear regression data are shown as dashed lines, and confidence intervals are shown as solid lines (slope ± s.d.).

**Table 1: Cell spreading area, volume and height.**

| Conditions | Mean cell area (µm²) | s.d. of the cell area (µm²) | Mean cell volume (µm³) | s.d. of the cell volume (µm³) | Cell height (µm) | s.d. of the height (µm) |
|---|---|---|---|---|---|---|
| siCRT- | 6,583 | 5,168 | 2,320 | 3,147 | 0.35 | 0.75 |
| siCRT+ | 9,025 | 7,258 | 2,710 | 4,326 | 0.30 | 0.72 |
| siCAV1- | 7,048 | 5,583 | 2,146 | 3,214 | 0.30 | 0.70 |
| siCAV1+ | 9,831 | 7,984 | 2,357 | 3,010 | 0.24 | 0.50 |
| siPTRF- | 7,539 | 5,450 | 1,914 | 2,234 | 0.25 | 0.48 |
| siPTRF+ | 10,139 | 7,873 | 2,282 | 2,628 | 0.23 | 0.43 |

The means and standard deviations (s.ds.) of the cell spreading area (Fig. 3C) and volume (Fig. 3D). Cell height was estimated by the ratio between the cell volume and cell area, and the standard deviation was estimated via error propagation.

# SUPPLEMENTARY MATERIALS

## Fig. S1. CAV1+/+ mice susceptibility to EDIN-B in Staphylococcal septicaemia.

Kaplan–Meier survival curves with data obtained through 7 days from groups of CAV1+/+ infected intravenously at Day 0 with different doses of LUG1799 wild-type *S. aureus*, expressed as colony-forming units per mouse (CFU/m). Comparative analysis of $CAV1^{+/+}$ mouse susceptibility to bloodstream infection with either the WT *edinB* or *ΔedinB* strain. Mice were injected with $5\times10^6$ CFU/m (n=5 mice infected with the WT *edinB* or *ΔedinB* strain; 1 experiment), 107 CFU/m (n=17 and n=19 mice infected with the WT *edinB* or *ΔedinB* strain, respectively; 3 experiments), $5\times10^7$ CFU/m (n=19 or n=18 mice infected with the WT *edinB* or *ΔedinB* strain; 3 experiments), and $5\times10^8$ CFU/m (n=4 or n=5 mice infected with either the WT or *ΔedinB* strain, respectively; 1 experiment). There were no significant differences in the kinetics of survival between the WT and *ΔedinB*-infected animals, as determined by log-rank test (Mantel–Cox).

## Fig. S2. Controls of siRNAs and RhoA ADP-ribosylation efficacies.

**(A)** Immunoblots show caveolin-1 (IB: CAV1) and cavin-1/PTRF (IB: PTRF) in total cellular extracts of HUVECs transfected with siCTRL and then treated for 24 h with ExoC3. Immunoblot GAPDH (IB: GAPDH) was used as the loading control. Immunoblots are representative of 3 independent experiments. **(B)** Immunoblots of caveolin-1 (IB: CAV1) and cavin-1/PTRF (IB: PTRF) show the specific and cross-depletion effects of siCAV1 and siPTRF. Immunoblot anti-GAPDH antibody (IB: GAPDH) shows equal loading. The graph shows caveolin-1 and cavin-1/PTRF levels normalized to the level of GAPDH (3 independent experiments). **(C)** Western blots show the fraction of ADP-ribosylated RhoA in cells that were resistant to a second round of in vitro ADP-ribosylation with biotin-NAD+. Western blot shows the fraction of ADP-ribosylated RhoA in vitro as detected with streptavidin–peroxidase (IB: Biotin-ADPr) i.e. not modified during cell intoxication. Immunoblotting with an anti-RhoA antibody (IB: RhoA) revealed equal RhoA protein levels. Immunoblotting with an anti-GAPDH antibody revealed equal protein loading. Blots are representative of n=3 independent experiments. The graph shows the mean values of the blot signal intensities ± s.ds. from n=3 independent experiments. Values correspond to the signal intensities of biotin-tagged ADP-ribosylated RhoA (Biotin-ADPr) normalized to those of RhoA and GAPDH IB signals. Values are expressed as a percentage compared with the intensity of the siCTRL-transfected untreated cells, which was set to 100%.

## Fig. S3. Caveolin-1 and cavin-1/PTRF depletion increases TEM formation in both ExoC3- and EDIN-treated cells.

**(A)** The graph shows the distribution of HUVECs between classes defined by TEM tunnel density ranging from a group of cells displaying only 1 TEM and those for which the density increased by a factor of 1 through those cells with 40 TEMs (y-axis). HUVECs were transfected with siCTRL, siCAV1 or siPTRF before treatment with ExoC3. The graph includes the geometric means ($N_{TEM}$) of the density of TEMs per cell within the whole cell population ± s.d. Graph shows technical replicates pooled together. Statistical data analysis using a mixed-effect linear model, with random intercept shows significant differences between values of $N_{TEM}$, ****P<0.0001. Data from *n*=1,400 cells per condition from 7 independent experiments. **(B)** Histograms show the percentages of EDIN-treated cells with at least one TEM (n=986 cells per treatment in 5 independent experiments). Error bars show 95% confidence intervals (CIs). Data analysis with a logistic regression model adjusted for multiple comparisons using Tukey's HSD test, ****P<0.0001; the siCTRL vs. siCAV1 groups and the siCTRL vs. siPTRF groups. No difference was recorded between the siCAV1 and siPTRF

groups. **(C)** The graph shows the distribution of HUVECs between classes as defined by TEM density with ranging from a group of cells displaying only 1 TEM and those for which the density increased by a factor of 1 through those cells with 40 TEMs (y-axis). HUVECs were transfected with siCTRL, siCAV1 or siPTRF before treatment with ExoC3. The graph includes values the geometric means ($N_{TEM}$) of the density of TEMs per cell within the whole cell population ± s.d. Statistical data analysis was based on a mixed linear model with a random intercept and fixed effects and revealed significant differences between $N_{TEM}$ values, ****P<0.0001 (n >986 cells per condition from 5 independent experiments).

**Fig. S4. Depletion of the caveolar accessory component EHD2 increases TEM formation.**

**(A)** Immunoblots show EHD2 cellular levels (IB: EHD2) in total cellular extracts of HUVECs transfected with siCTRL or siEHD2 and then treated for 24 h with ExoC3. Immunoblot GAPDH (IB: GAPDH) was used as the loading control. Immunoblots are representative of n=3 independent experiments. **(B)** Histograms show the percentages of C3-treated cells displaying at least one TEM (n=1000 cells per condition from 5 independent experiments). Error bars show 95% confidence intervals (CIs). Data analysis with a logistic regression model adjusted for multiple comparisons using Tukey's HSD test, ****P<0.0001 for the siCTRL versus siEHD2 groups. **(C)** The graph shows the distribution of HUVECs between classes as defined by TEM density ranging from a group of cells displaying only 1 TEM and those for which the density increased by a factor of 1 through those cells with 40 TEMs/cell (y-axis). HUVECs were transfected with siCTRL or siEHD2 before treatment with ExoC3. The graph includes values of the geometric means ($N_{TEM}$) of the density of TEMs per cell within the whole cell population ± s.d. Statistical data analysis was based on a mixed linear model with a random intercept and fixed effects and revealed significant differences between $N_{TEM}$ values, ****P<0.0001 (n= 1000 cells per condition from 5 independent experiments).

**Fig. S5. Caveolin-1 controls the TEM opening speed and maximum size.**

The graph shows variations in TEM areas as a function of time expressed in minutes. HUVECs transfected with siCTRL, siCAV1 or siPTRF were treated for 24 h with ExoC3. (n> 22 TEMs per condition; 4 biological replicates). Experimental data were obtained via a video recorded at 1 frame/second for 30 minutes.

Figure 1

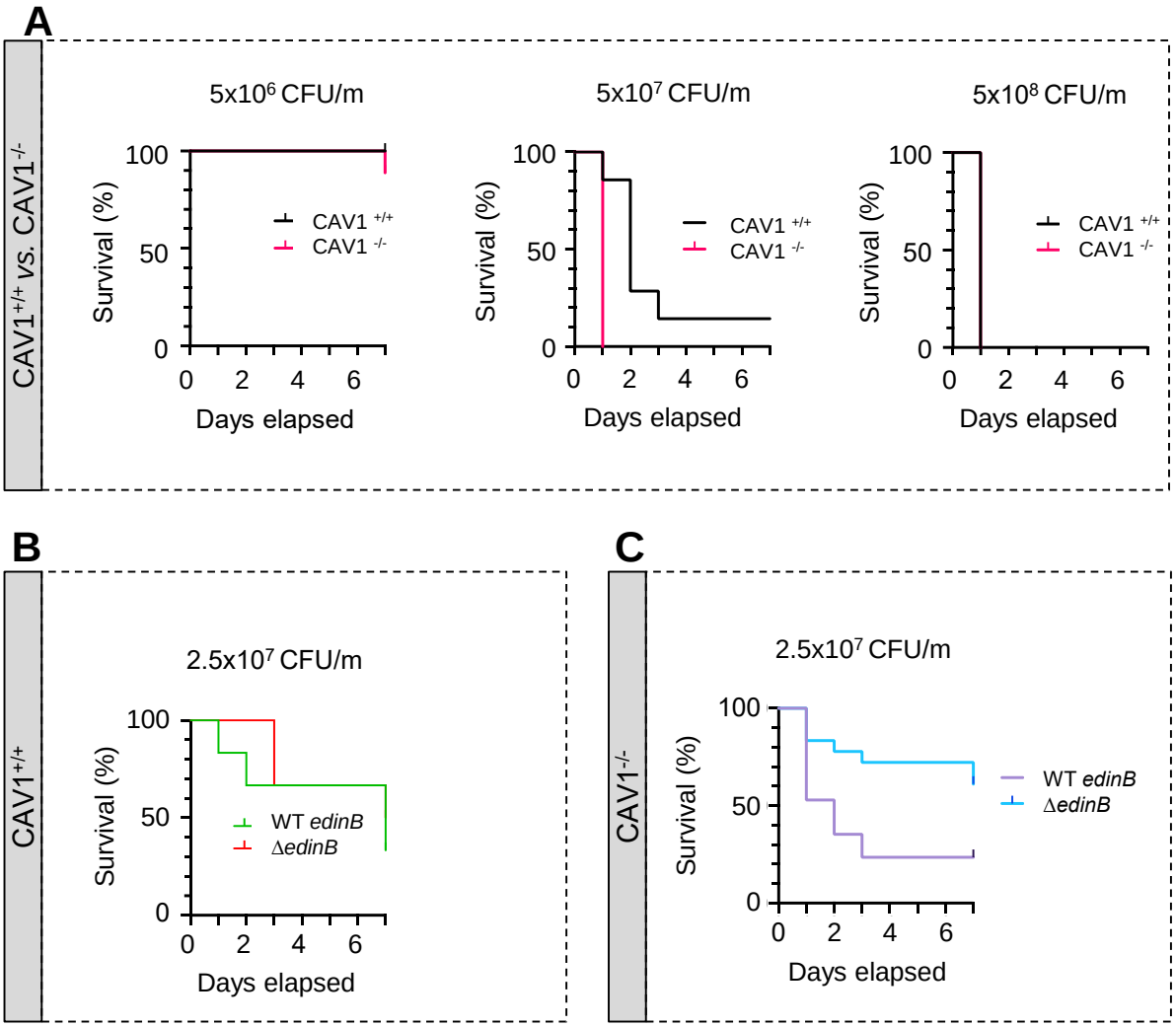

Figure 2

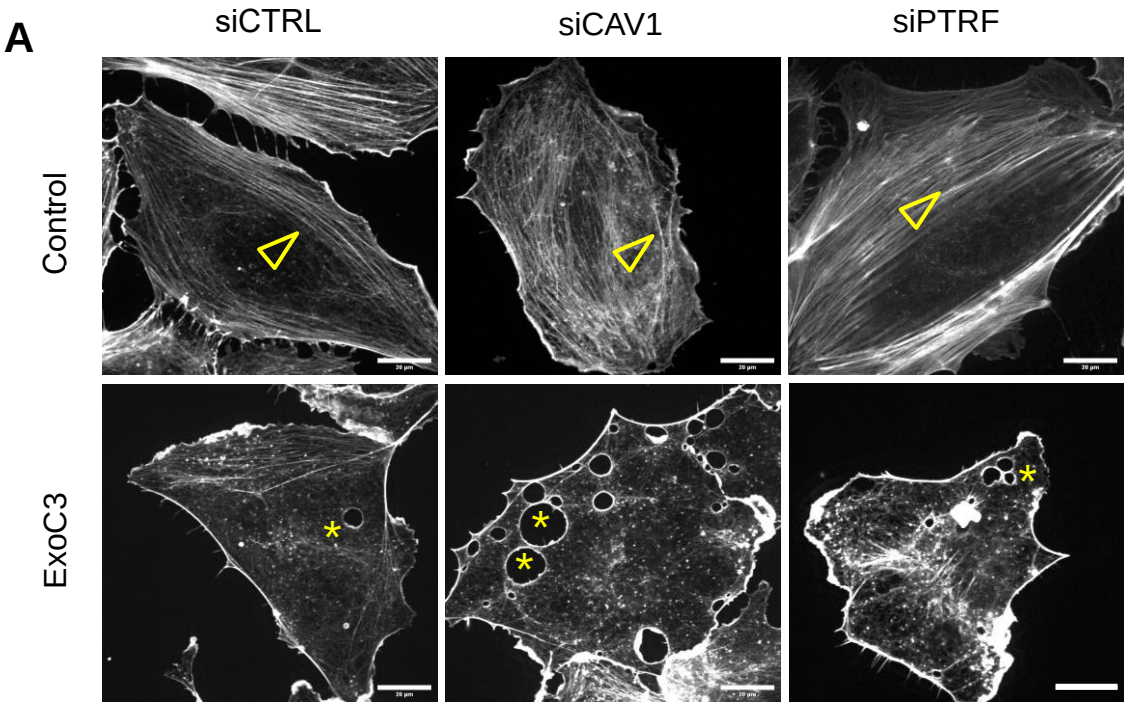


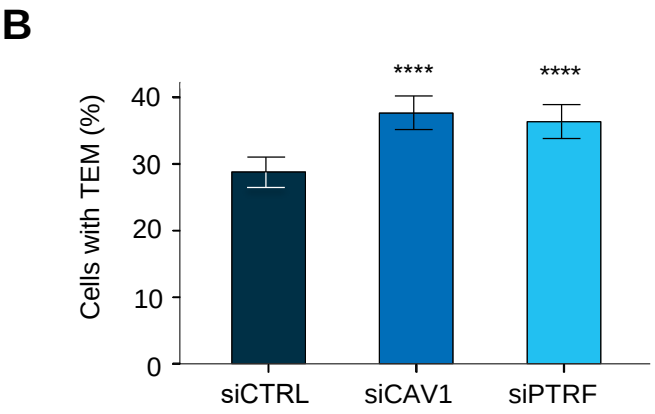

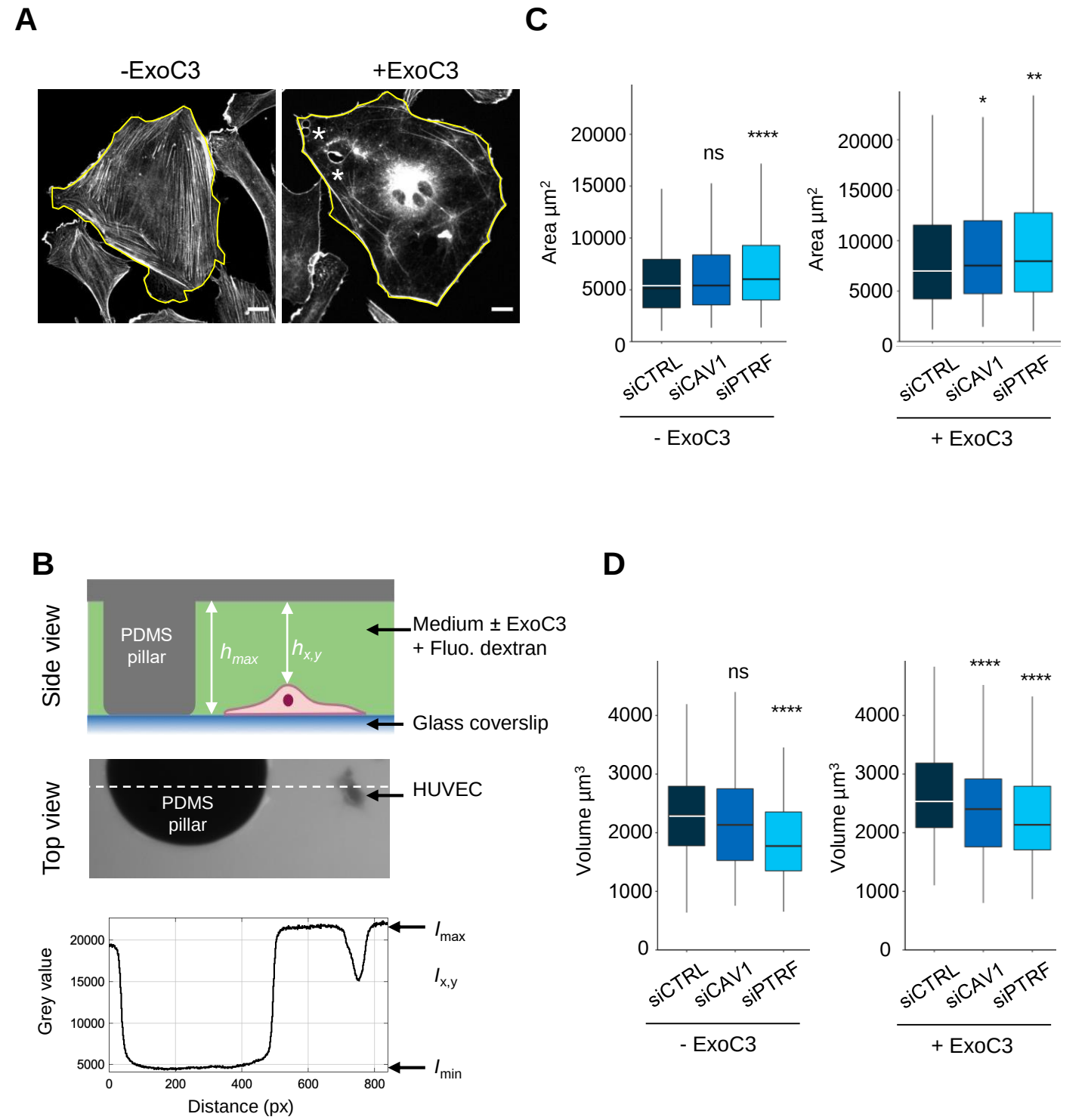

Figure 4

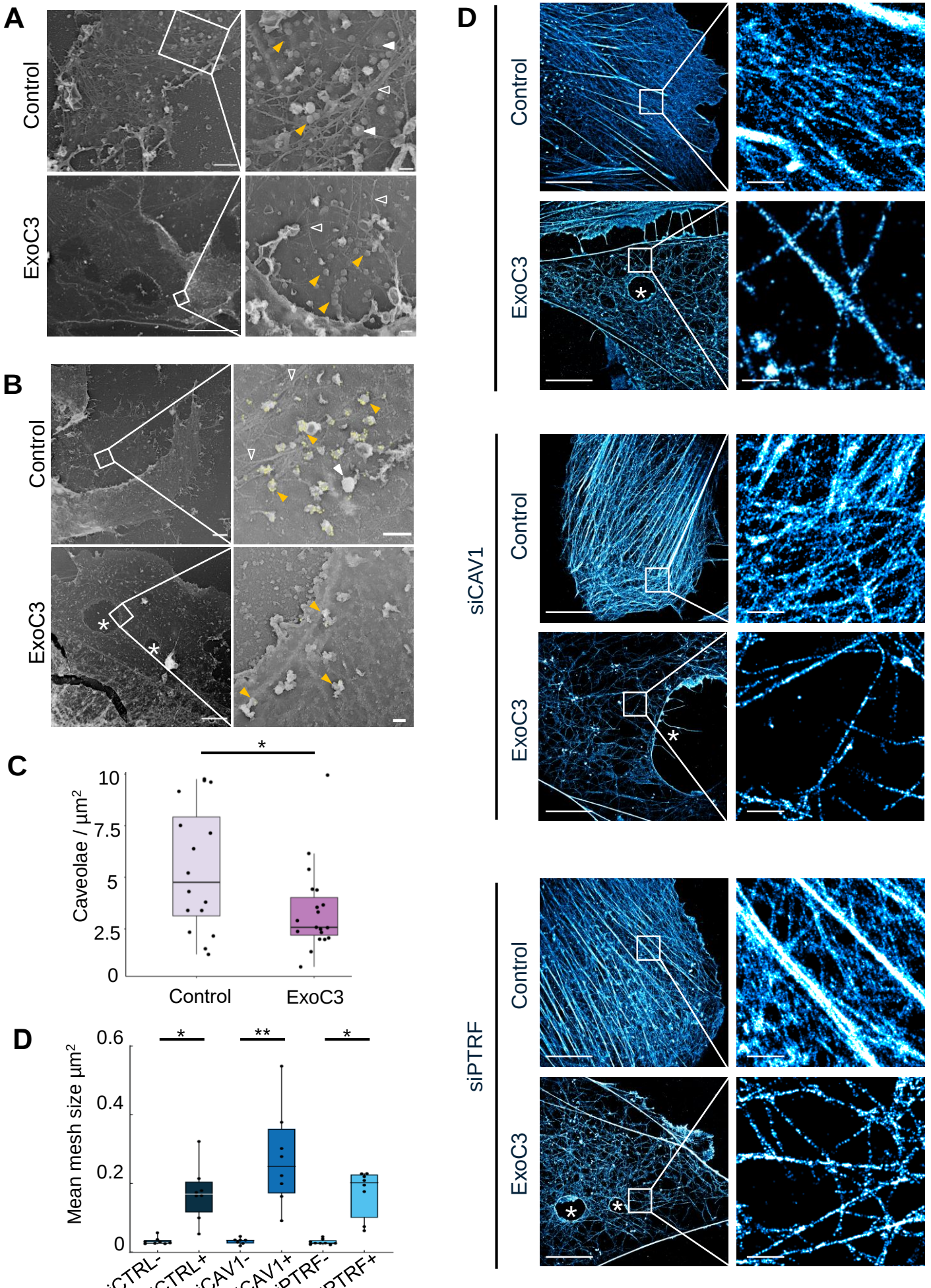

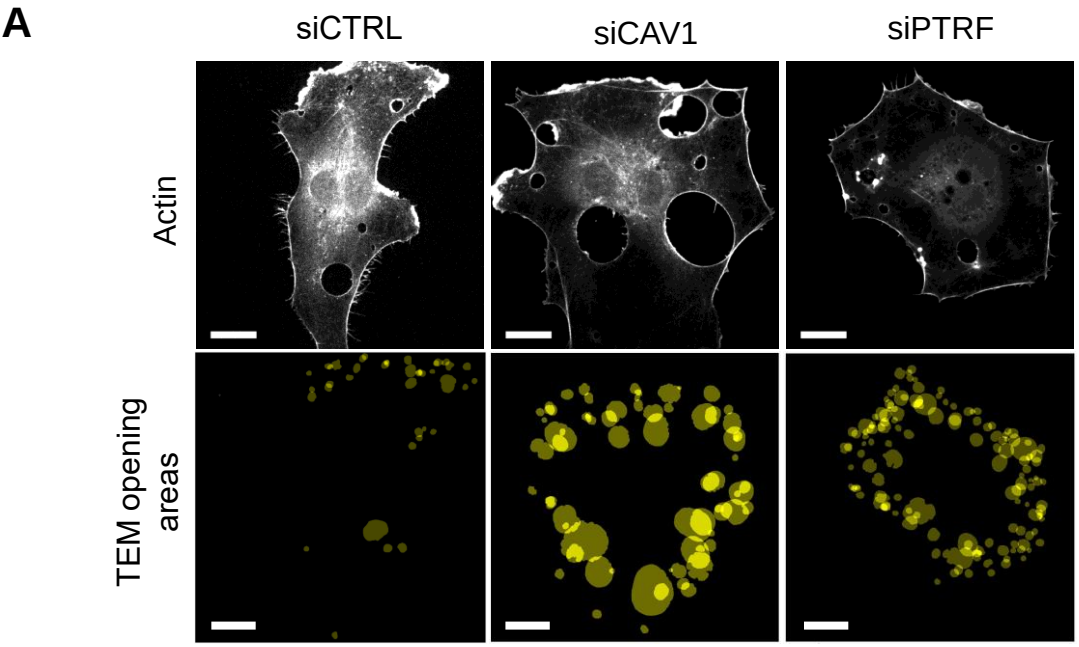


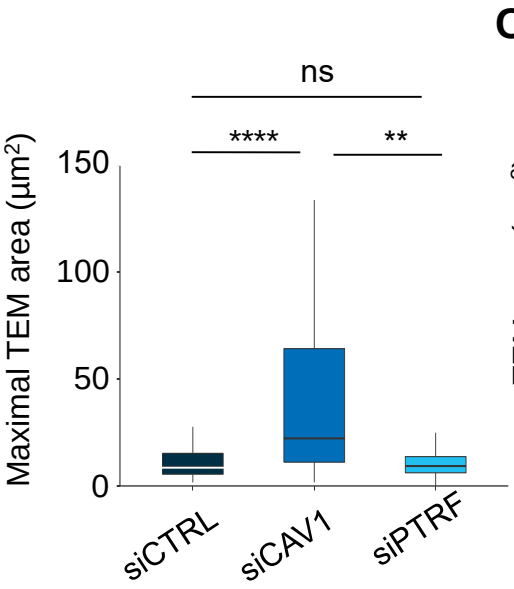


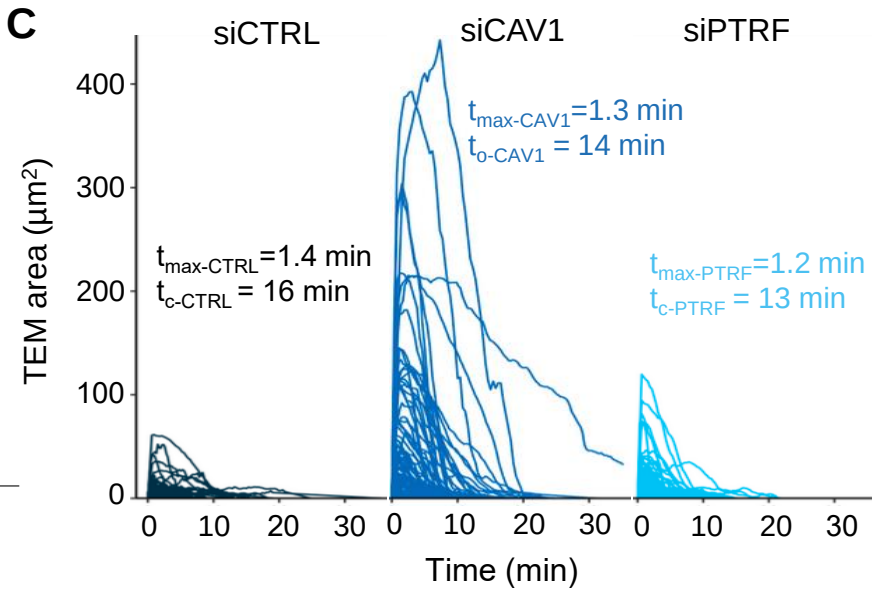


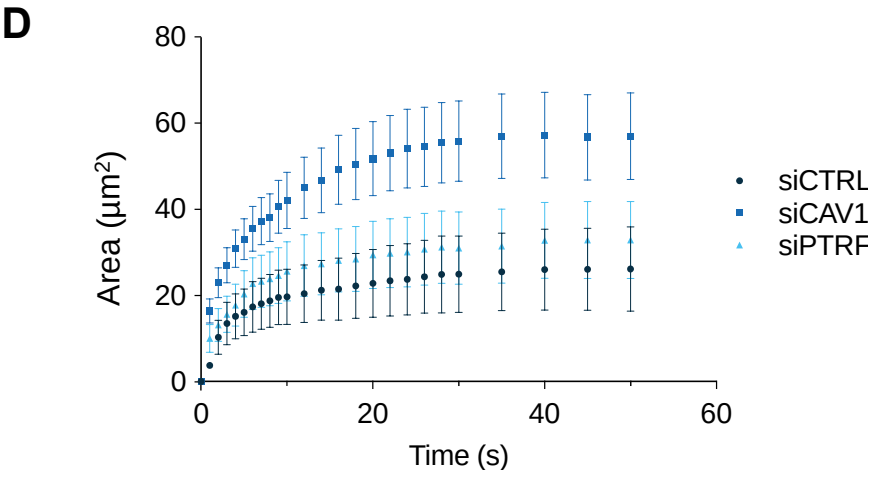

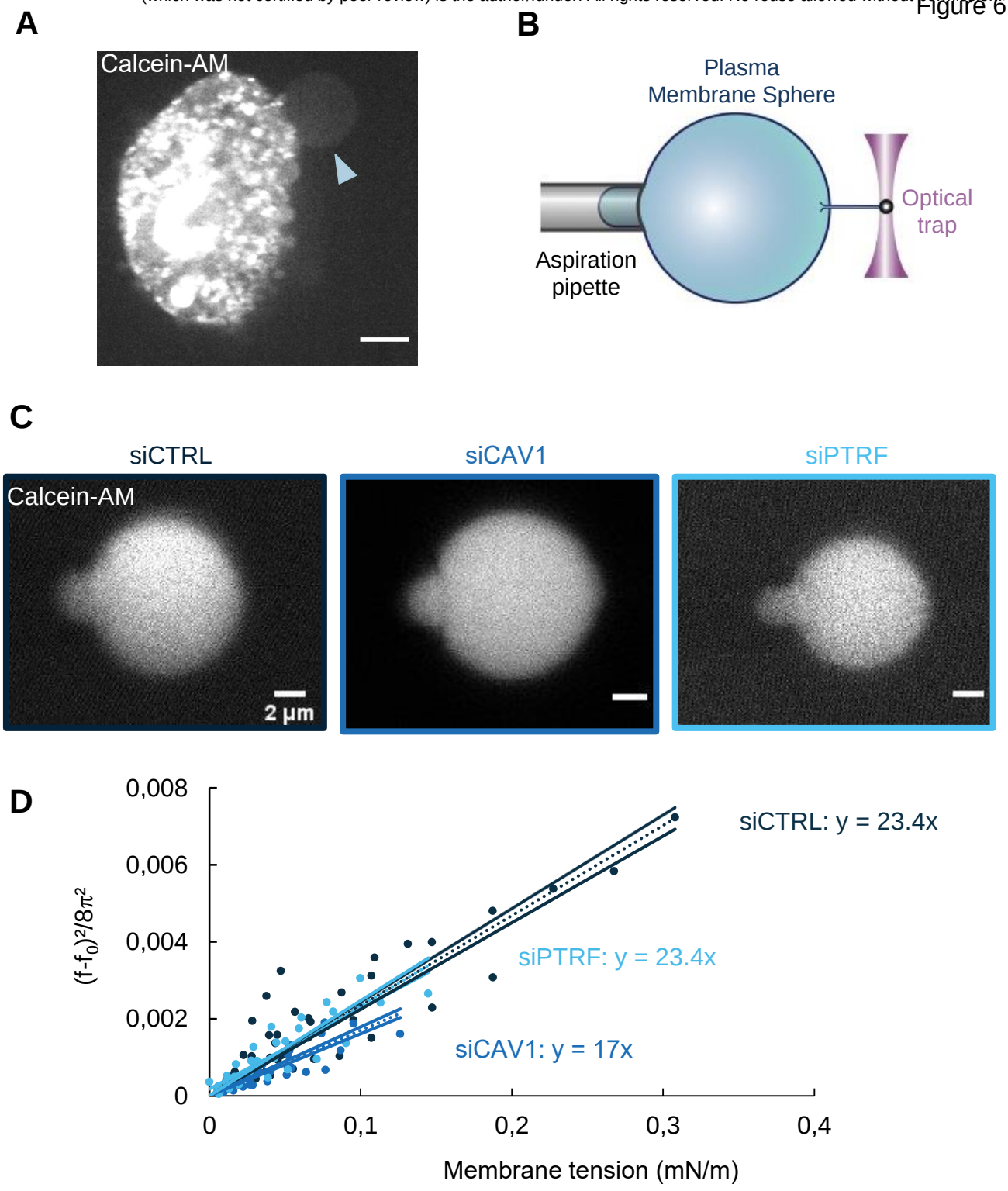

Figure S1

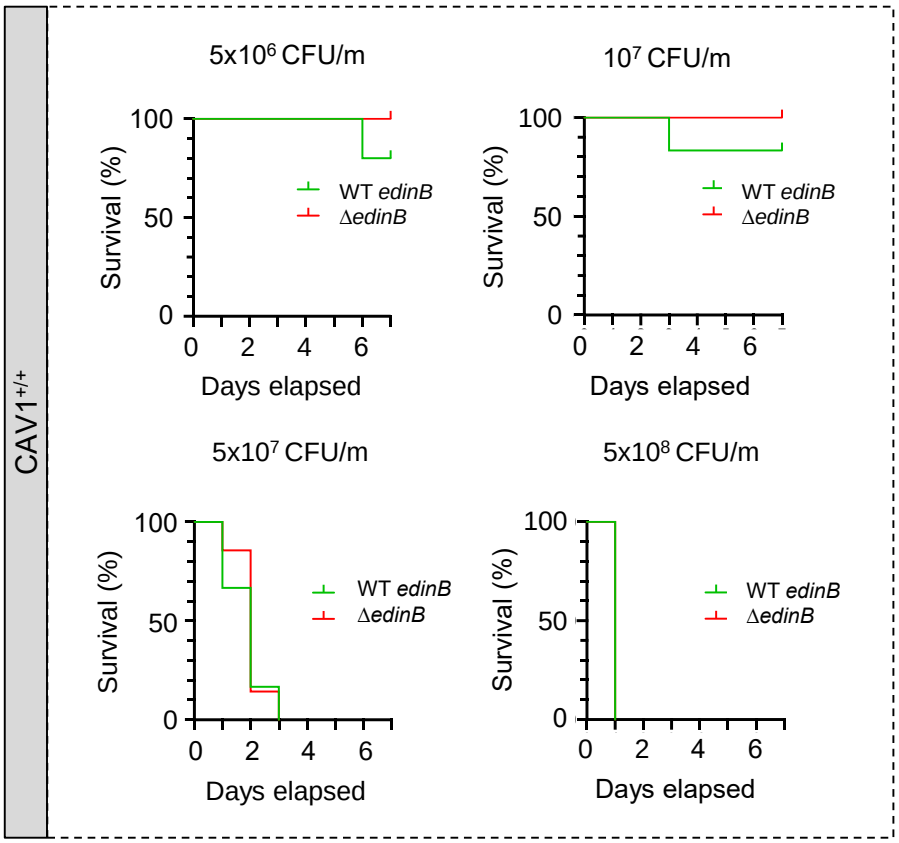

Figure S2

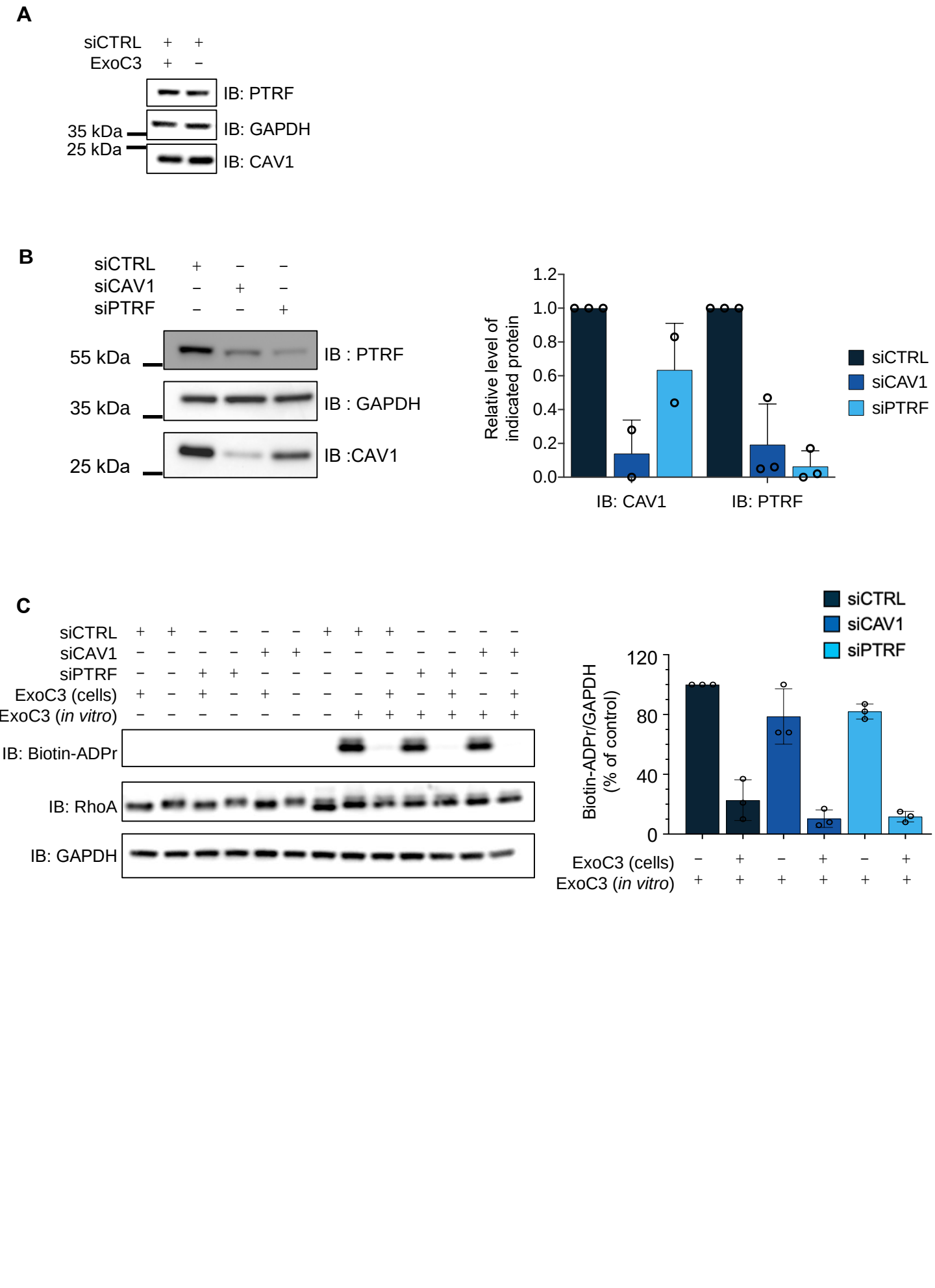

Figure S3

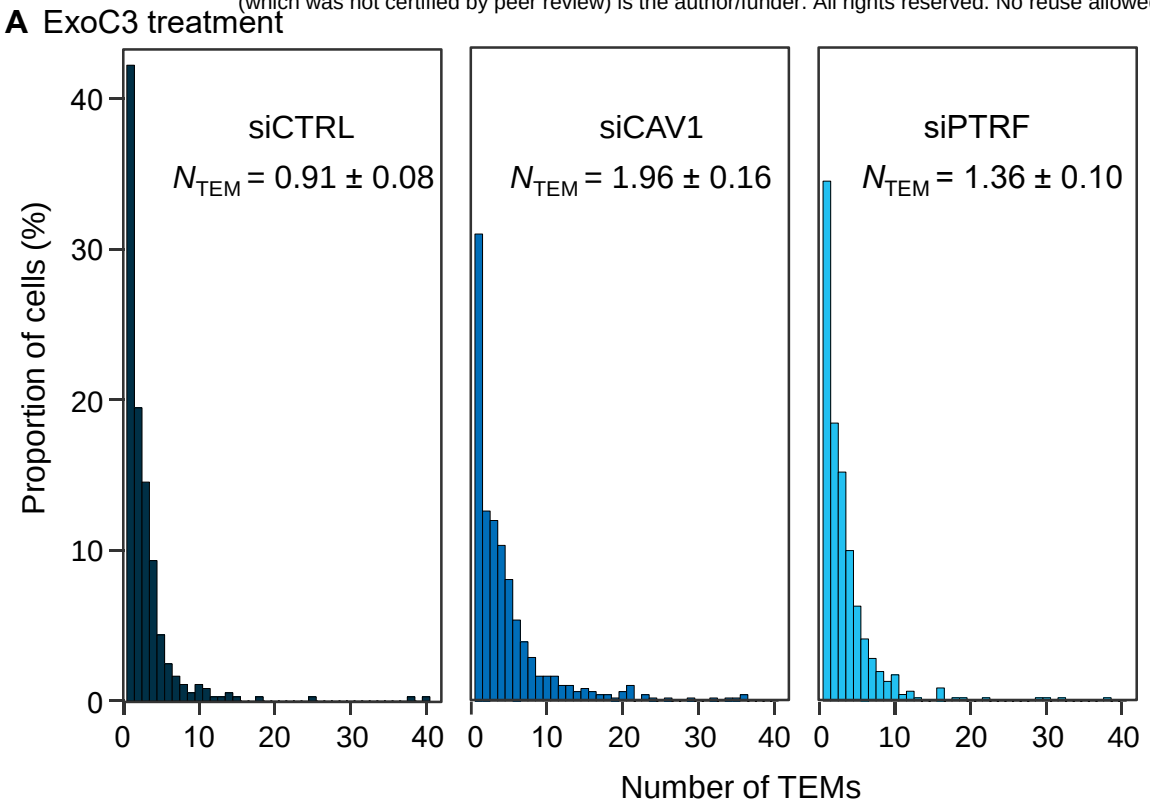


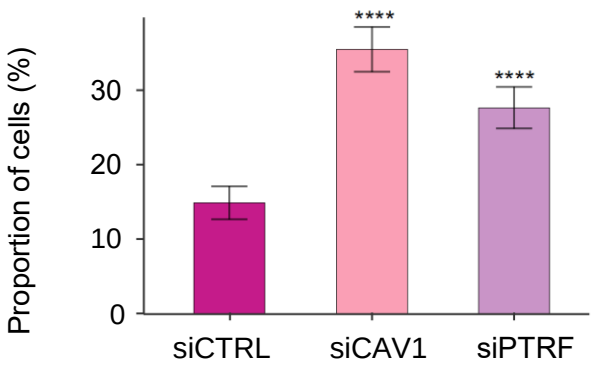


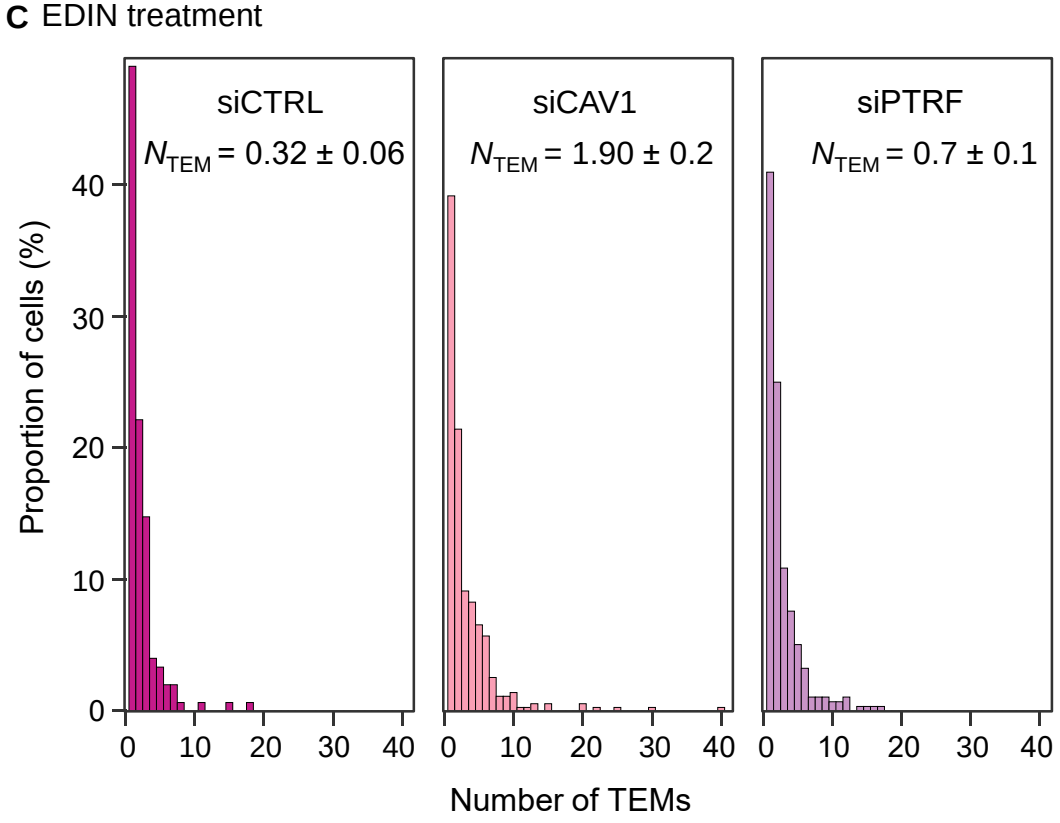

Figure S4

**A**

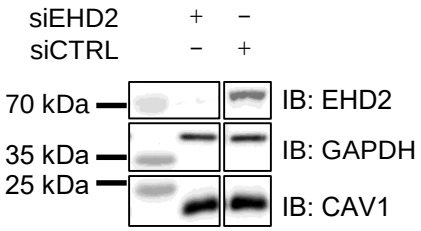


**B** ExoC3 treatment

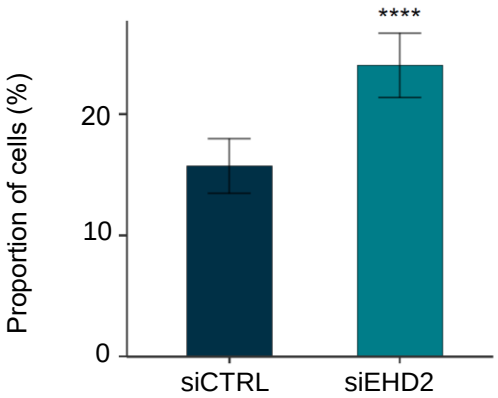


**C** ExoC3 treatment

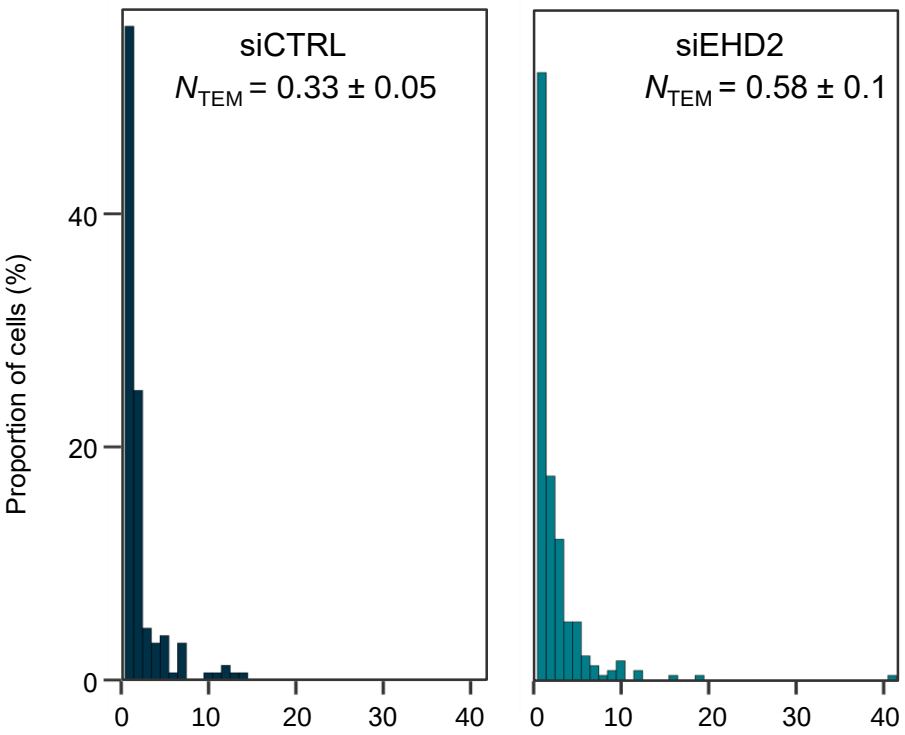

Figure S5